

## Optimal resolution tomography with error tracking and the structure of the crust and upper mantle beneath Ireland and Britain

Raffaele Bonadio<sup>1</sup>, Sergei Lebedev<sup>1</sup>, Thomas Meier<sup>2</sup>, Pierre Arroucau<sup>3</sup>, Andrew J. Schaeffer<sup>4</sup>, Andrea Licciardi<sup>5</sup>, Matthew R. Agius<sup>6</sup>, Clare Horan<sup>1</sup>, Louise Collins<sup>1</sup>, Brian M. O'Reilly<sup>1</sup>, Peter W. Readman<sup>1</sup> and the Ireland Array Working Group\*

<sup>1</sup>Dublin Institute for Advanced Studies, Dublin, Ireland. E-mail: [bonadio@cp.dias.ie](mailto:bonadio@cp.dias.ie)

<sup>2</sup>Christian-Albrechts-Universität zu Kiel, Inst. for Geosciences, Kiel, Germany

<sup>3</sup>EDF-DIPNN-DI-TEGG, Aix-en-Provence, France

<sup>4</sup>Geological Survey of Canada, Sidney, Canada

<sup>5</sup>Université Côte d'Azur, Geoazur, Sophia Antipolis, France

<sup>6</sup>Dipartimento di Scienze, Università Roma Tre, Roma, Italy

Accepted 2021 April 19. Received 2021 April 13; in original form 2020 October 6

### SUMMARY

The classical Backus–Gilbert method seeks localized Earth-structure averages at the shortest length scales possible, given a data set, data errors, and a threshold for acceptable model errors. The resolving length at a point is the width of the local averaging kernel, and the optimal averaging kernel is the narrowest one such that the model error is below a specified level. This approach is well suited for seismic tomography, which maps 3-D Earth structure using large sets of seismic measurements. The continual measurement-error decreases and data-redundancy increases have reduced the impact of random errors on tomographic models. Systematic errors, however, are resistant to data redundancy and their effect on the model is difficult to predict. Here, we develop a method for finding the optimal resolving length at every point, implementing it for surface-wave tomography. As in the Backus–Gilbert method, every solution at a point results from an entire-system inversion, and the model error is reduced by increasing the model-parameter averaging. The key advantage of our method stems from its direct, empirical evaluation of the posterior model error at a point. We first measure inter-station phase velocities at simultaneously recording station pairs and compute phase-velocity maps at densely, logarithmically spaced periods. Numerous versions of the maps with varying smoothness are then computed, ranging from very rough to very smooth. Phase-velocity curves extracted from the maps at every point can be inverted for shear-velocity ( $V_S$ ) profiles. As we show, errors in these phase-velocity curves increase nearly monotonically with the map roughness. We evaluate the error by isolating the roughness of the phase-velocity curve that cannot be explained by any Earth structure and determine the optimal resolving length at a point such that the error of the local phase-velocity curve is below a threshold. A 3-D  $V_S$  model is then computed by the inversion of the composite phase-velocity maps with an optimal resolution at every point. The estimated optimal resolution shows smooth lateral variations, confirming the robustness of the procedure. Importantly, the optimal resolving length does not scale with the density of the data coverage: some of the best-sampled locations display relatively low lateral resolution, probably due to systematic errors in the data. We apply the method to image the lithosphere and underlying mantle beneath Ireland and Britain. Our very large data set was created using new data from Ireland Array, the Irish National Seismic Network, the UK Seismograph Network and other deployments. A total of 11 238 inter-station dispersion curves, spanning a very broad total period range (4–500 s), yield unprecedented data coverage of the area and provide fine regional resolution from the crust to the deep asthenosphere. The lateral

\*<https://www.irelandarray.ie>

resolution of the 3-D model is computed explicitly and varies from 39 km in central Ireland to over 800 km at the edges of the area, where the data coverage declines. Our tomography reveals pronounced, previously unknown variations in the lithospheric thickness beneath Ireland and Britain, with implications for their Caledonian assembly and for the mechanisms of the British Tertiary Igneous Province magmatism.

**Key words:** Tomography; Structure of the Earth; Surface waves and free oscillations; Inverse theory; Time-series analysis; Seismic interferometry.

## 1 INTRODUCTION

Seismic tomography uses measurements made on seismograms to produce 3-D models of Earth interior, at scales from local to regional to global (e.g. Aki & Lee 1976; Dziewonski *et al.* 1977; Nolet 2008). The 3-D models are solutions of one or a series of inverse problems. Normally, we would like the models to have the highest possible spatial resolution.

### 1.1 Resolution

Resolution is a fundamental concept in seismic tomography and other imaging fields. It is generally understood as a measure of the ability of an instrument or an experiment to distinguish adjacent features from one another (e.g. Abbe 1873; Helmholtz 1874; Rayleigh 1896; Feynman *et al.* 1963; Köhler 1981; Sheriff & Geldart 1995). The specific definitions and the limits of the resolution vary with the data type and the design of the image-forming system, from microscopy and telescopy (e.g. Abbe 1873; Helmholtz 1874; Rayleigh 1896) to spectroscopy (McNaught & Wilkinson 2014) and to reflection seismology (Sheriff & Geldart 1995). The term resolution is used widely and in many ways, and its specific meaning can be ambiguous even within the same field (e.g. den Dekker & van den Bos 1997; Demmerle *et al.* 2015). We thus start with a brief summary on the usage and with definitions.

The classic work on the subject focused on the resolving power of a telescope or a microscope for a self-luminous double point (Abbe 1873; Helmholtz 1874; Rayleigh 1896). A point source, such as a star, is broadened by diffraction into a finite-width circle on the image. The Rayleigh criterion states that the minimum separation between two light sources required for them to be resolved as distinct objects is proportional to the wavelength of the wave and inversely proportional to the device's aperture (Rayleigh 1896). The specific limit of resolution predicted by the Rayleigh criterion may not necessarily be reached in practice due to noise, depending on the experimental conditions (Ronchi 1961).

The smallest resolvable interval is the angular spread in telescopy, the wavelength or wavenumber difference in optical spectroscopy and the spatial distance in seismic imaging. In all cases, an actual point source or point anomaly broaden into a finite-width feature on the image (Fig. 1), so that similar natural definitions of the resolution apply (e.g. Feynman *et al.* 1963). In reflection seismology, for example, the quarter-wavelength resolution criterion is the equivalent of and is often referred to as the Rayleigh criterion (Sheriff & Geldart 1995).

Seismic tomography differs from telescopy or microscopy in that the image is computed, rather than observed. The resolution, understood as our ability to distinguish features on the image, generally has a complex, non-linear dependence on the data sampling and errors in the data. In their pioneering early work, Backus & Gilbert (1968, 1970) developed a method for computing accurate localized averages of the Earth structure at the shortest length scales that

a given data set, with its given errors, can resolve at given points. Their method determines, for a point  $\mathbf{r}_0$ , an optimal averaging kernel that is most nearly like  $\delta(\mathbf{r}_0 - \mathbf{r})$  (Backus & Gilbert 1970).

Backus & Gilbert (1968) defined the resolving length as the width of the peak of the optimal averaging kernel. In their treatment of errors, Backus & Gilbert (1970) assumed that the variance matrix of the measurement errors can be estimated, and computed the statistics of the resulting model errors using the statistics of the data errors and error-propagation theory.

In this paper, we define the resolving length as the full width at the half-maximum of an averaging kernel at a point (Fig. 1). The averaging kernel is estimated using a point-spread function at the point, computed in a test inversion with the only anomaly being a spike anomaly at this point and with the inversion formulated exactly as that of the real data (Yanovskaya 2005; Oldenborger & Routh 2009; Fitchner & van Leeuwen 2015; Celli *et al.* 2020). These empirical averaging kernels describe the spreading of spike anomalies  $\delta(\mathbf{r}_0 - \mathbf{r})$  in space. The shape of the kernels is not postulated *a priori*. With our inversion set-up, the kernels turn out to have a natural bell shape, close to a Gaussian in cross-section (Section 3.3). This resolving length definition is similar to that using the half-width of a cone, illustrated and applied in a number of previous tomography studies (e.g. Barmin *et al.* 2001; Ritzwoller *et al.* 2002; Lebedev *et al.* 2003; Celli *et al.* 2020).

The resolving length is equal to the distance above which two spike anomalies can be distinguished (Fig. 1). The resolution of the imaging is said to be higher if the resolving length is shorter, and lower if the resolving length is greater. The term resolution is also often used with the meaning of the resolving (averaging) length—as in, for example, ‘resolution of 100 km’ (Nolet 2008, p. 221).

In linear inverse theory, resolution is often discussed in terms of the closeness of the resolution matrix to the identity matrix. For a linear inverse problem

$$\mathbf{A}\mathbf{m} = \mathbf{d}, \quad (1)$$

where  $\mathbf{m}$  is the model vector,  $\mathbf{d}$  the data vector and  $\mathbf{A}$  the sensitivity matrix, the solution  $\mathbf{m}$  can be written as

$$\mathbf{m} = \mathbf{A}^{-1}\mathbf{d}, \quad (2)$$

where  $\mathbf{A}^{-1}$  is a generalized inverse (e.g. Nolet 2008; Menke 2012). Substituting eq. (1) into eq. (2),

$$\mathbf{m} = \mathbf{A}^{-1}\mathbf{A}\mathbf{m}^{(\text{true})} = \mathbf{R}\mathbf{m}^{(\text{true})}, \quad (3)$$

where  $\mathbf{R} = \mathbf{A}^{-1}\mathbf{A}$  is the model resolution matrix. It can be thought of as a blurring filter through which we see the real Earth ( $\mathbf{m}^{(\text{true})}$ ) on the tomographic image.

If the observed data  $\mathbf{d}$  is the sum of the error-free data  $\mathbf{d}^{(\text{true})}$  and data errors  $\mathbf{e}$ , then the error of the solution  $\mathbf{m}$  is (Nolet 2008):

$$\begin{aligned} \mathbf{m} - \mathbf{m}^{(\text{true})} &= \mathbf{A}^{-1}\mathbf{d} - \mathbf{m}^{(\text{true})} = (\mathbf{A}^{-1}\mathbf{A} - \mathbf{I})\mathbf{m}^{(\text{true})} + \mathbf{A}^{-1}\mathbf{e} \\ &= (\mathbf{R} - \mathbf{I})\mathbf{m}^{(\text{true})} + \mathbf{A}^{-1}\mathbf{e}. \end{aligned} \quad (4)$$

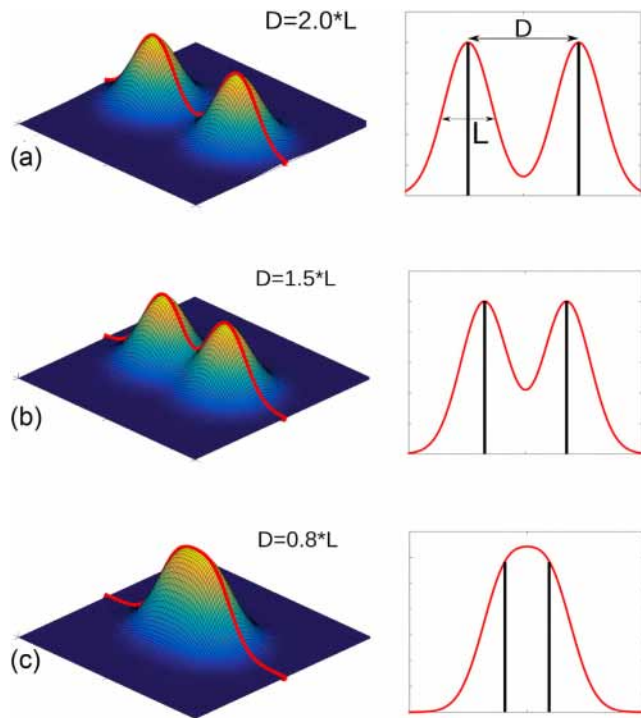


**Figure 1.** Schematic illustration of the averaging kernel and the resolving length. The resolving (averaging) length  $L$  is defined as the full width of the local averaging kernel at its half maximum. Resolving length equals the distance  $D$  between two point anomalies above which they can be distinguished on the image as separate.

Two components of the model error are the blurring of the true structure by the tomographic ‘filter’, quantified by the difference of the resolution matrix and the identity matrix ( $\mathbf{R} - \mathbf{I}$ ), and the propagated data errors  $\mathbf{A}^{-1}\mathbf{e}$ .

An additional, third component of the model error comes from the error of the linear relationship  $\mathbf{A}\mathbf{m} = \mathbf{d}$  itself. If the parameters of the model  $\mathbf{m}$  sample a 3-D volume or a 2-D plane, then the  $i$ th row of the matrix  $\mathbf{A}$  defines the sensitivity volume or sensitivity area assigned to the measurement  $d_i$ , specifying the weights of the model parameters within this volume or area. The sensitivity volumes depend on the measurement method and on the imperfectly known structure of the Earth (Dahlen & Tromp 1998) and are, at best, a good approximation. Errors may also result from the problem linearization itself (e.g. Rawlinson *et al.* 2010).

If the off-diagonal elements of  $\mathbf{R}$  are all zero, then each parameter is determined uniquely. In practice, they are usually non-zero, so that the parameters are weighted averages of the true model parameters. One measure of the resolution  $\mathbf{R}$  is the net size, or the spread, of the off-diagonal elements (Menke 2012).

The broadening of a point anomaly in the model (Fig. 1) is described by the leakage from the diagonal to off-diagonal elements of the resolution matrix. The averaging kernel of a tomographic inversion, estimated using a point-spread function, yields an approximation of a row or a column of the model resolution matrix (Ritzwoller *et al.* 2002; Menke 2015). Point-spread functions computed for every parameter of the model yield an estimate of the entire resolution matrix and a map of the resolving lengths (Ritzwoller *et al.* 2002; Celli *et al.* 2020). The definition of resolution in terms of ( $\mathbf{R} - \mathbf{I}$ ) is thus similar to its definition in terms of our ability to distinguish adjacent features. An important difference is that  $\mathbf{R}$  is independent of errors in the data and approximations (Menke 2012), whereas the optimal averaging kernels—and our ability to

distinguish adjacent features from one another—do depend on the errors (Backus & Gilbert 1970).

## 1.2 Errors

As the resolving length decreases, the error of the localized average increases (Backus & Gilbert 1970). The trade-off of the resolution and variance is a general principle of inverse theory: the resolution spread can be decreased at the expense of increasing the variance, and vice versa (Menke 2012).

The model variance arises from the incompleteness of the data sampling and from the errors in the data and the methods’ approximations. The growth in the coverage of the Earth with seismic stations over the last few decades has driven a continuous increase in the resolution of global and regional tomographic models (e.g. Rawlinson *et al.* 2010). Errors of most types have also decreased, and the increasing data redundancy is reducing the impact of random, uncorrelated errors. In many cases, however, the remaining errors are systematic, so that their effect on the models is resistant to the data-redundancy increase.

For example, in tomography using teleseismic delay times or phase delays accumulated between sources and stations, the major source of errors is the uncertainty in the event location and origin time and, for waveform analysis techniques, of the source mechanisms. The source parameters in published catalogues were computed using approximate, assumed Earth structure, and their errors in a given source region tend to be systematic (Lebedev *et al.* 1997; Bijwaard *et al.* 1998). Differential measurements, including inter-station, surface-wave measurements as in this study, isolate the information on local structure from the effect of the source but tend to have complex sensitivity volumes, shaped by structural heterogeneity both near and away from the stations (e.g. de Vos *et al.* 2013) and impossible to map exactly. Measurement errors due to instrumental errors—timing errors, response-correction errors, polarity reversals—remain a problem (e.g. Weidle *et al.* 2013; De Laet *et al.* 2019) and are also systematic.

The errors in the data propagate into errors in the models and limit the resolution of the imaging via the resolution-variance trade-off (Backus & Gilbert 1970; Menke 2012). In order to keep the model error below a certain level, the resolving length must be sufficiently large. Comparisons of different global tomographic models give a vivid illustration of this trade-off: the models show an excellent mutual agreement at long spatial wavelengths but a progressively decreasing agreement at decreasing wavelengths (e.g. Boschi & Dziewonski 1999; Becker & Boschi 2002; Schaeffer & Lebedev 2015; Schaeffer *et al.* 2016).

## 1.3 Spatially variable resolution

The optimal averaging-kernel width (Backus & Gilbert 1968) varies spatially because of the unevenness of the data sampling and error distribution. The unevenness of the data coverage is due to the irregular geographical distribution of the sources and receivers.

A number of approaches have been implemented to accommodate the spatially variable level of detail in model (Rawlinson *et al.* 2010). Irregular parametrizations aim to place the nodes of the grid only where they are required by the data, or have the size of the blocks scaled with data sampling (e.g. Chou & Booker 1979; Tarantola & Nercessian 1984; Fukao *et al.* 1992; Sambridge *et al.* 1995; van der Hilst *et al.* 1997; Bijwaard *et al.* 1998; Bijwaard & Spakman 2000; Debayle & Sambridge 2004; Zhao 2004; Sambridge & Rawlinson



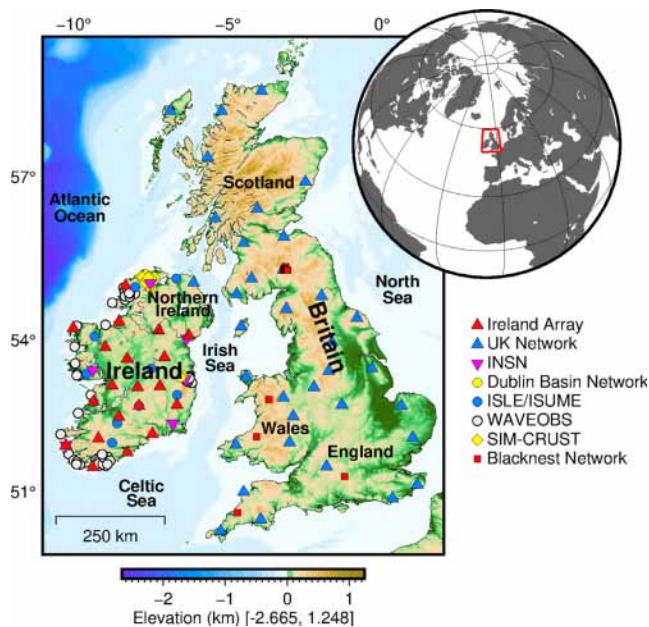


**Figure 2.** The seismic stations in Ireland and Britain used in this study belong to Ireland Array (Lebedev *et al.* 2012), the UK Seismograph Network operated by the British Geological Survey (e.g. Baptie 2018), the Irish National Seismic Network (INSN) (INSN 1993; Blake *et al.* 2012), the Dublin Basin temporary network (Licciardi & Piana Agostinetti 2014), the ISLE and ISUME projects (Landes *et al.* 2004; Do *et al.* 2006; Landes *et al.* 2007; Wawerzinek *et al.* 2008; O'Donnell *et al.* 2011; Polat *et al.* 2012), the WAVEOBS project (Möhlhoff & Bean 2016), the SIM-CRUST project (Piana Agostinetti & Licciardi 2015) and the Blacknest Array (AWE 2020). Topography and bathymetry are from the GEBCO data set (IOC *et al.* 2003).

2005). The grid density can vary according to chosen indicators of the resolving power of the data at different locations, such as hit counts or sensitivity-matrix column sums. The inversion can be parametrized using nested grids, with a higher-resolution grid where the sampling is greater or in the area of primary interest—for example, a denser grid for a region embedded into a sparser global grid. Adaptive parametrization aims to adjust in the course of the inversion, matching the spatially varying structural information yielded by the data (e.g. Michelini 1995; Curtis & Snieder 1997; Sambridge & Faletić 2003; Rawlinson & Kennett 2004). Recently, dynamic parametrizations in Bayesian frameworks without explicit regularization have been developed and applied to tomographic and other seismic-data inversions (e.g. Bodin & Sambridge 2009; Piana Agostinetti & Malinverno 2010; Bodin *et al.* 2012; Piana Agostinetti *et al.* 2015; Galetti *et al.* 2016; Hawkins *et al.* 2019).

Commonly used forms of regularization of tomographic inversions with local parametrizations are norm damping and smoothing, with the smoothing implemented, typically, as gradient damping or Laplacian damping or both (e.g. Nolet 2008; Lebedev & van der Hilst 2008). Lateral and radial smoothing increases the width of the averaging kernels and decreases the nominal resolution of the models. The resolution varies spatially even in inversions with constant factors of regularization, because the same regularization term has a smaller effect where the data coverage is denser and the data-misfit term is greater (e.g. Nolet 2008). The spatially varying resolution can be examined using resolution tests (e.g. Rawlinson & Spakman 2016) or resolution-matrix calculations (e.g. Boschi 2003; Deschamps *et al.* 2008), but neither of the approaches can quantify the impact of unknown, correlated errors in the data.

## 1.4 Optimal resolution tomography

Backus & Gilbert (1970) formulated and solved the problem of how to find the shortest length scale over which local average structure at a particular point can be determined with the variance under a specified amount. In other words, they determined the optimal resolving length (the width of the peak of their optimal averaging kernel), or optimal resolution, given the errors.

The Backus–Gilbert averaging kernels were used in a number of mantle tomography studies (e.g. Trampert & van Heijst 2002). Beyond that, their work has been a major influence on the geophysical inverse theory (e.g. Chou & Booker 1979; Tarantola & Nercessian 1984; Parker 1994; Nolet 2008; Menke 2012) and inspired the development of optimally localized average (OLA) methods in other fields. The computationally efficient Subtractive Optimally Localized Averages (SOLA) method (Pijpers & Thompson 1994), popular in helioseismology, has recently been adapted to seismic tomography by Zanolli (2016, 2019) and Zanolli *et al.* (2017).

In this study, we pose the problem in the same way as Backus & Gilbert (1968, 1970): how can we find the solution of the tomographic inverse problem with the smallest resolving length at every point, such that the error of the local average at the point is below a specified threshold? We recognize that the statistics of the errors in the data and approximations are unknown. From what we know about the errors, we can say that they are unlikely to have a zero mean and are substantially correlated, in ways that are unlikely to be guessed or modelled accurately. This makes them difficult to handle using error-propagation estimation used in the linear inverse theory (Nolet 1985).

But what if we had a way to evaluate the posterior model error at a point directly? With that, we could solve the inverse problem repeatedly, adjusting the width of the averaging kernel at this point until the error is just below the specified threshold. In other words, we would be able to determine the optimal resolution at the point. Similarly to the Backus–Gilbert method, this would reduce the variance by increasing the volume over which the model parameter is averaged, until the error is acceptable. Like in the Backus–Gilbert method, every estimate at a point would require a full inversion of the entire system—a series of inversions, in fact.

The key advantage of this approach over the existing ones stems from its key ingredient, the direct evaluation of the model error. In the following, we develop the optimal resolution tomography for the surface-wave tomography problem, set up as a sequence of phase-velocity tomography and the point-by-point inversion of local phase-velocity curves. We shall start with presenting our large regional data set, introduce the phase-velocity measurements and, then, describe the implementation and validation of the optimal resolution tomography, with an application to the imaging of the crust and upper mantle beneath Ireland and Britain.

## 1.5 Imaging Ireland and Britain

The lithospheric evolution of the Ireland–Britain region (Tiley *et al.* 2004; Landes *et al.* 2007; Holland & Sanders 2009; Davis *et al.* 2012; Cogné *et al.* 2016) and the mechanism of its enigmatic Palaeogene intraplate volcanism (White & Lovell 1997; Jones *et al.* 2002; Al-Kindi *et al.* 2003) are poorly understood, in large part due to the lack of information on the region's lithospheric structure. Much of our present knowledge of the seismic structure of the crust beneath Ireland and Britain is from active source seismic refraction and reflection experiments (Bamford *et al.* 1978; Edwards & Blundell 1984; Bott *et al.* 1985; Jacob *et al.* 1985; Freeman *et al.* 1988; Lowe & Jacob 1989; Snyder & Flack 1990; Klemperer & Hobbs 1991;

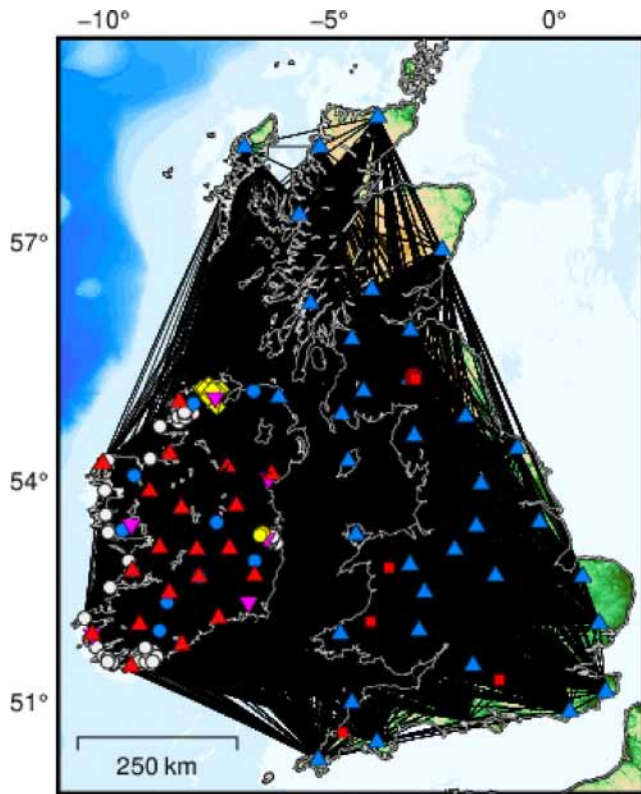


**Figure 3.** Station locations (as in Fig. 2) and the inter-station path coverage (black lines) yielded by our measurements. The coverage in Ireland is denser than in Britain due to data availability.

Klemperer *et al.* 1991; Barton 1992; O'Reilly *et al.* 1996, 2012; Masson *et al.* 1998; Landes *et al.* 2000; Hodgson 2001; Kelly *et al.* 2007; O'Reilly *et al.* 2010; Maguire *et al.* 2011). Maps of the Moho depth have been obtained from the results of the active-source experiments and, also, by combining them with those from receiver functions (e.g. Chadwick & Pharaoh 1998; Asencio *et al.* 2003; Landes *et al.* 2005; Kelly *et al.* 2007; Di Leo *et al.* 2009; Davis *et al.* 2012; Licciardi *et al.* 2014, 2020).

Passive-source investigations of the region's crust and upper mantle included teleseismic traveltimes comparisons (Masson *et al.* 1999), teleseismic body-wave tomography (Arrowsmith *et al.* 2005), local earthquake tomography (Hardwick 2008), receiver-function (Shaw Champion *et al.* 2006; Tomlinson *et al.* 2006; Landes *et al.* 2007; Davis *et al.* 2012; Licciardi *et al.* 2014) and shear-wave splitting (Do *et al.* 2006; Bastow *et al.* 2007) analysis and surface-wave tomography (Polat *et al.* 2012; Nicolson *et al.* 2012, 2014; Galetti *et al.* 2016). Magnetotelluric and gravity studies provided additional, complementary information (Brown & Whelan 1955; Readman *et al.* 1997; Rao *et al.* 2007). Recently, petrological modelling and inversion were applied to integrate seismic, geothermal, compositional and magnetic data (Fullea *et al.* 2014; Jones *et al.* 2013; Mather *et al.* 2018; Baykiev *et al.* 2018; Mather & Fullea 2019).

The coverage of Ireland with seismic stations was sparse and uneven until recently. Regional surface-wave studies to date (Polat *et al.* 2012; Nicolson *et al.* 2012, 2014; Galetti *et al.* 2016) focused on parts of the region and used data in limited period ranges. Continent-scale tomographic models typically include Ireland and

Britain at the edge of the model, imaged with relatively low resolution (e.g. Marquering & Snieder 1996; Fry *et al.* 2008; Schivardi & Morelli 2009; Rickers *et al.* 2013; Soomro *et al.* 2016).

## 2 DATA AND MEASUREMENTS

In this study, we used the abundant, newly available data in the Ireland–Britain region in order to obtain numerous phase-velocity measurements in very broad frequency ranges (from periods as short as 4 s to those as long as 500 s) and to image the entire region at a new level of detail. We used phase-velocity measurements, generally more accurate than group-velocity ones (e.g. Meier *et al.* 2004; Boschi *et al.* 2013; Soomro *et al.* 2016) and yielding more accurate maps (Dahlen & Zhou 2006). The phase-velocity dispersion curves were obtained for 11 238 two-station paths across the area using a combination of a recent implementation of the two-station method and waveform inversion. Our data set includes all the data recorded by the broadband networks in Ireland and all the publicly available data from the broadband stations in Britain (Appendix A1). In total, our measurements were made on data recorded between 1981 and 2018, but the bulk of the data is from the last decade. Thanks to the recent growth in the number of stations, especially in Ireland, our data set provides an unprecedentedly dense data coverage of the entire region (Figs 2 and 3).

The waveform data went through automated quality checks and pre-processing. The integrity of the data was ensured by removing all the data that were incomplete, clipped, had gaps. The seismograms were converted to displacement by the removal of the instrument response and down-sampled to 1 Hz.

### 2.1 Teleseismic two-station cross-correlation

For each available station pair, we searched the Global Centroid Moment Tensor catalogue (Dziewonski *et al.* 1981; Ekström *et al.* 2012) for teleseismic events within the operating time period of the two stations and with a chosen back-azimuth range of  $\pm 5^\circ$  from the station–station great circle path (GCP). Events with a moment magnitude greater than 4.9 were chosen, using a distance-dependent magnitude threshold (Schaeffer & Lebedev 2013). Only Rayleigh-wave data from the vertical component were used for the measurements; Love wave measurements will be incorporated in a future study.

The use of the two-station method, as introduced by Sato (1955), in surface-wave analysis allows us to compute phase-velocity dispersion of the surface waves that travel approximately along the GCP between stations of a pair. It is possible to make a regional investigation using teleseismic earthquakes, since the phase effects of the source (earthquake) and the common path between the source and the receivers cancel out (e.g. Meier *et al.* 2004; Soomro *et al.* 2016). In practice, the waves from a given earthquake do not travel exactly along the GCP, so we need to allow a certain tolerance for the alignment between the earthquake and the pair of stations. This tolerance can be chosen depending on the availability and quality of the data. In this paper, the low threshold of  $\pm 5^\circ$  is chosen, due to high availability of recordings and relatively high signal-to-noise ratios. Such conservative data-selection approach is allowed by the enormous quantity of available waveforms, in contrast to other studies in which the threshold has to be higher, due to a smaller quantity of available data and a lower signal-to-noise ratio of recordings (e.g. Bonadio *et al.* 2018).

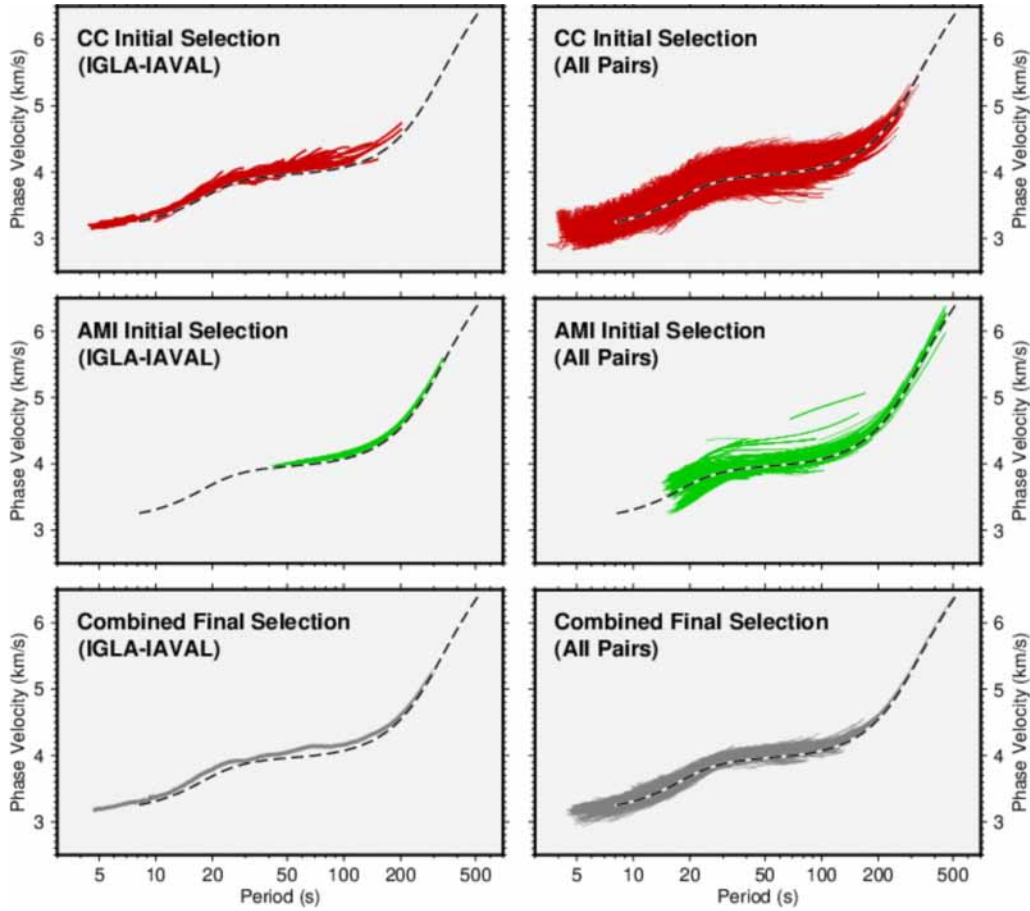


**Figure 4.** Phase-velocity curves measured with the two-station cross-correlation and waveform inversion. Left-hand panel: the single-event, two-station dispersion measurements for the pair IGLA–IAVAL. Right-hand panel: the measurements for all the station pairs. Top panels: cross correlation measurements. Middle: waveform inversion measurements. Bottom panels: the final phase-velocity curves computed as averages over all the measurements from the two methods for the station pair. Only the portions of the curves with at least 10 single-event measurements at each period are included.

Although the tolerance around the station-station GCP is very small, one may argue that the misalignment may have a non-negligible effect on the accuracy of the calculated phase velocity. However, the imperfect alignment of the two stations and the event has no immediate effect on the measurement accuracy because the phase velocities are computed from the phase of the cross-correlation function and the difference between the distances from the event to each of the stations, rather than the inter-station distance between the two-stations (e.g. Soomro *et al.* 2016).

In this work, we use the implementation of the two-station method by Meier *et al.* (2004). The automated measurement procedure is adapted for our particular data set from Soomro *et al.* (2016). For each teleseismic event, the vertical component seismograms recorded at the two stations are cross-correlated. The cross-correlation signal is then filtered using a frequency-dependent Gaussian bandpass filter, so as to minimize the effect of noise and interferences on the fundamental mode. The resulting signal is then weighted in the time domain to reduce the effects of scattering and higher modes. The phase velocity is computed from the resulting signal in the Fourier domain as the arctangent of the ratio of the imaginary to real part of the Fourier spectrum. This

approach works best if the fundamental mode is dominant compared to any other type of signal or noise in its vicinity on the traces.

The accuracy of the resulting curve depends on the amplitude of the fundamental mode content, the signal-to-noise ratio, unmodelled surface-wave diffraction, and the interferences of the Rayleigh and Love, fundamental and higher modes. The smaller the errors due to the diffraction and interferences, the more accurate and the smoother the dispersion curve. To minimize the effect of the errors in the curves on the final, average measurements, we only accept smooth portions of phase-velocity curves. We also exclude the outlier measurements and, also, accept only the curves not unrealistically far from a pre-calculated reference dispersion curve (how the reference curves used in this work are computed is discussed in Section 2.3). The accepted phase-velocity segments are selected subject to the following criteria (e.g. Soomro *et al.* 2016):

(i) Segments that present a low number of samples are not selected for the final averaging; due to the logarithmic sampling of the frequency axis the minimum acceptable length of the segments varies with period (i.e. longer segments are accepted at longer periods, while shorter segments may be accepted at shorter periods).



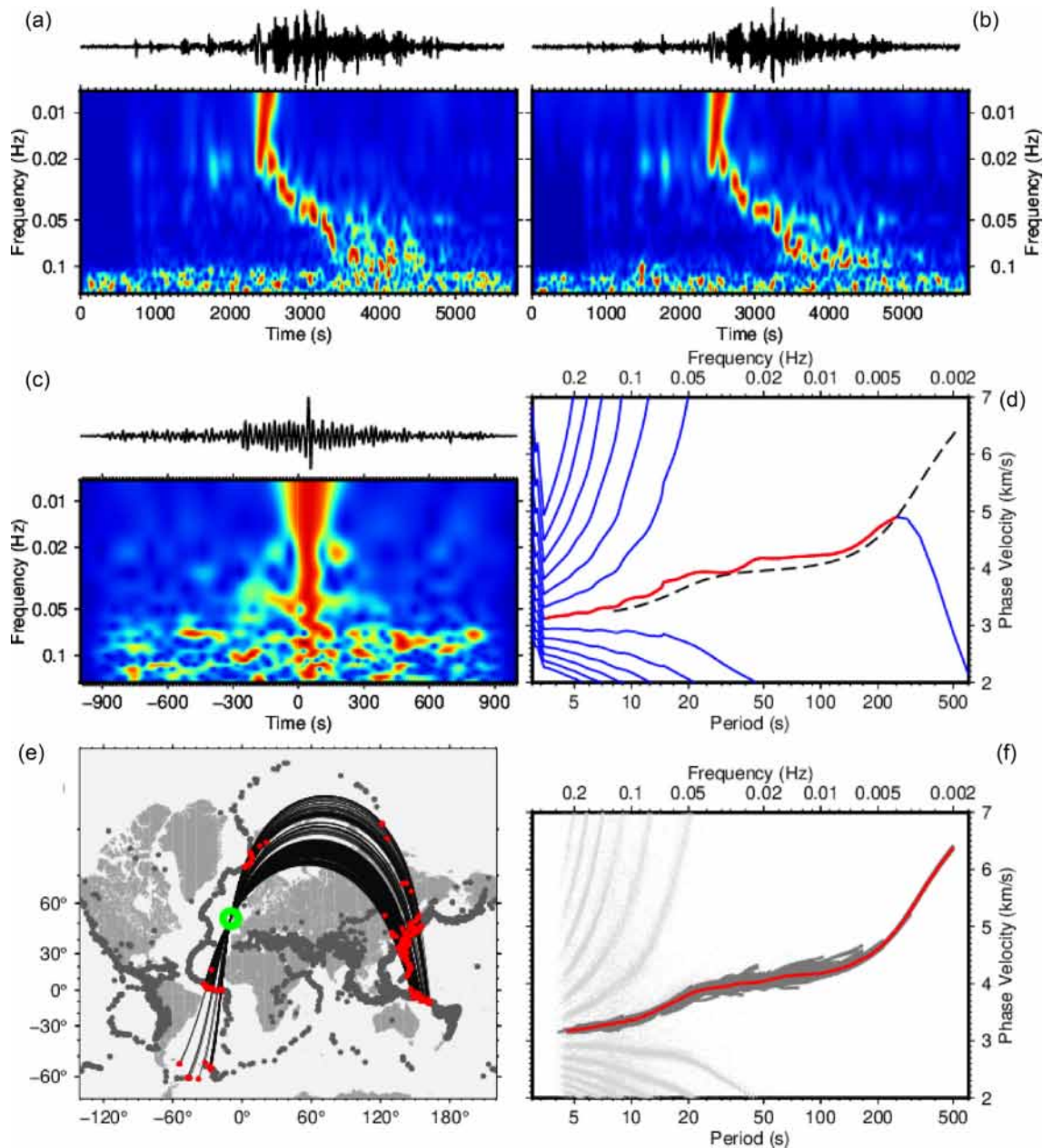


**Figure 5.** Example of an inter-station, Rayleigh-wave, phase-velocity measurement for the station pair IGLA–IAVAL. Both IGLA and VAL are INSN stations in western Ireland, and IAAVAL was an Ireland Array station collocated with VAL and operated before a broadband INSN instrument was installed at the site. Panels (a) and (b) show the recorded seismograms and the time–frequency representations of their waveforms. Panel (c) the cross-correlation signal and its time–frequency representation. Panel (d) phase-velocity curves measured in the frequency domain by unwrapping the phase of the cross-correlation function (Section 2.1). Alternative curves resulting from the  $2\pi$  ambiguity are plotted in blue. The accepted segment is shown in red. Dashed line: AK135 (Kennett *et al.* 1995). Panel (e) all the events used in this study (grey), the events used for this pair of stations (red) and the great circle paths between these events and the stations. The locations of the two stations are within the green circle. Panel (f) the accepted one-event, phase-velocity measurements (dark grey lines) and the final measurement for the station pair (red), computed by averaging over all cross-correlation and waveform inversion measurements. The light grey dots indicate the branches of measurements affected by the  $2\pi$  ambiguity, relative to the accepted one-event, phase-velocity measurements shown with dark grey lines. The event that yielded the data in (a)–(d) is an  $M_w = 7.32$  earthquake located at  $38.56^\circ\text{N}$ ,  $142.78^\circ\text{E}$ , at a depth of 14.1 km. The station IGLA (at  $53.42^\circ\text{N}$ ,  $9.38^\circ\text{W}$ ) is  $84.92^\circ$  away from the event, with a backazimuth  $21.56^\circ$ . The station IAAVAL ( $51.94^\circ\text{N}$ ,  $10.24^\circ\text{W}$ ) is  $86.49^\circ$  away from the event, with a backazimuth  $20.87^\circ$ . The inter-station distance is 174.5 km.

(ii) For each pair of stations, the ensemble of selected curves is analysed for the number of measurements at each period; if a minimum number of measurements (10 in this study) has not been reached, the measurements at those periods are not included into the final data set.

(iii) If a systematic inconsistency between measurements from events at opposite directions from the station pair is detected, the measurements from the station-pair are removed from the data set. The procedure computes the average phase velocity and the standard deviation for each set of measurements corresponding to the two

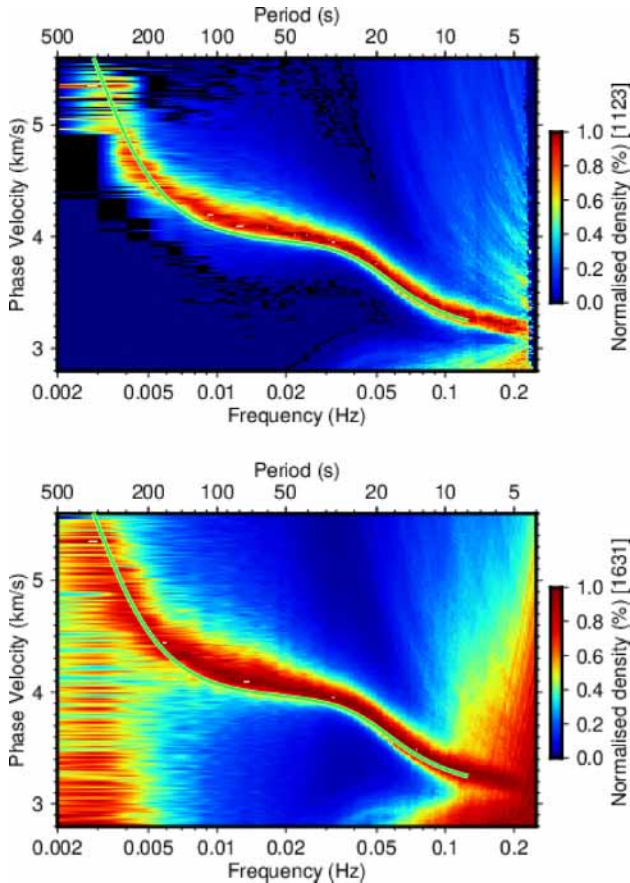


**Figure 6.** Determination of a reference dispersion curve. Bottom: The stack of all initial phase-velocity measurements in the region, with no selection applied, already shows a fairly accurate, region-average phase-velocity curve (Section 2.3). The stack is computed using all branches of possible phase-velocity curves, including those affected by the  $2\pi$  ambiguity, for all pairs of stations. The branches that do not represent the real Earth structure tend to cancel out in the stack. Top panel: the stack obtained via a loose selection of preliminary measurements (Section 2.3), shows an improvement compared to the stack obtained from all measurements (bottom panel) and yields an accurate reference model for the definitive, one-by-one phase-velocity measurement selection. Both density plots are normalized to the maximum at each frequency. Green lines: AK135 (Kennett *et al.* 1995).

directions, and the measurements are rejected if the phase-velocity difference for the two directions exceeds a certain threshold. It is important not to introduce this inconsistency in the data, as this effect could indicate instrumental errors (station timing or instrument response) or strong diffraction effects. In the data set in this study, the procedure has not detected any station pair displaying such inconsistency.

We used all station pairs with inter-station distances greater than 1 km and within the area of the map in Figs 2 and 3. For each station pair, we computed an average over, typically, many tens to a few hundreds of one-event measurements, made using recordings of earthquakes in different source regions, in different directions from the station pair. The averaging over a large number of measurements reduces the effect of errors due to diffraction and interferences between the fundamental and higher modes and results in robust average measurements in very broad period ranges. The automatic

selection described applies to the measurements obtained with both the two-station cross-correlation (CC) and the automated multimode inversion (AMI, Section 2.2).

## 2.2 Measurements from waveform inversion

We use the automated multimode inversion of surface and  $S$ -wave forms (Lebedev *et al.* 2005) to complement our phase-velocity measurements at intermediate and long periods. The AMI method simultaneously fits  $S$ , multiple  $S$  and surface waves for each source–station pair, using synthetic seismograms generated by mode summation in seismogram-dependent time–frequency windows. As a by-product of the waveform inversion, it measures phase velocities within the period bands constrained by this particular waveform fit. For each source–receiver pair, we extracted the fundamental-mode phase velocities. We then used pairs of stations at the same azimuth from the event ( $\pm 5^\circ$ ) to calculate the inter-station phase velocity using the relation

$$c_{12} = \frac{\Delta_2 - \Delta_1}{\Delta_2/c_2 - \Delta_1/c_1}, \quad (5)$$

where  $c_{i=1,2}$  and  $\Delta_{i=1,2}$  are the phase velocity and the distance between the source and each of the two stations, respectively, and  $c_{12}$  is the inter-station phase velocity (Lebedev *et al.* 2006; Agius & Lebedev 2014). The advantage of using AMI for inter-station measurements and combining them with those obtained by cross-correlation is that the waveform inversion can measure phase velocities at long periods, where the cross-correlation often fails because of the strong interference between surface and body waves (e.g. Meier *et al.* 2004; Zhang *et al.* 2009; Agius & Lebedev 2013).

With these two automated methods, we computed a very large number of phase-velocity, inter-station curves in a total period range of 4–500 s (Fig. 4). The measurements generated by the different techniques (at short, intermediate and long periods—by cross-correlation, and at intermediate and long periods—by waveform inversion) are consistent where they overlap. The curves from cross-correlation and AMI are averaged all together (Section 2.1). The final set of measurements used for the construction of the velocity maps (Section 3) is shown in Fig. 4. The period range of the final data set is 4–500 s.

## 2.3 Reference model for the measurements

A  $\pm 2\pi$  ambiguity arises when phase velocities are computed from the cross-correlation function (e.g. Meier *et al.* 2004; Soomro *et al.* 2016; Bonadio *et al.* 2018; El-Sharkawy *et al.* 2020). We need a reference model to discriminate the curves that represent the true Earth structure from the ones that are shifted up or down by the trigonometric ambiguity. For longer periods, identifying the correct dispersion curve is normally straightforward (Fig. 5d). The ambiguity may occur, instead, at higher frequencies, where the choice of the correct curve is not always trivial, with the curves close to each other. Using an accurate *a priori* reference phase-velocity curve is thus important for the phase-velocity measurements. It would not work, for example, to use a global reference model such as AK135 (Kennett *et al.* 1995) or PREM (Dziewonski & Anderson 1981) if the study area presents substantially different phase-velocity dispersion compared to these models.

We computed a reference model for the region using the method of Bonadio *et al.* (2018), which provides a data-based initial reference curve for the area. Stacking together all possible phase-velocity curves derived from cross-correlations for the



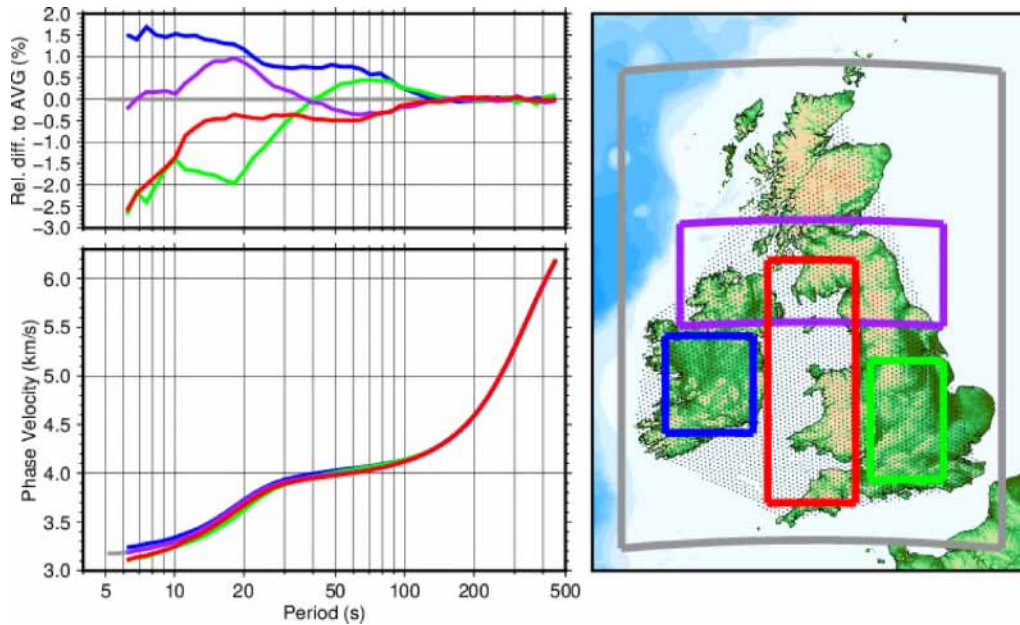


**Figure 7.** Lithospheric heterogeneity in the region seen in the differences between the subregion-average, phase-velocity curves. The region-average dispersion curves are computed using the optimal-resolution, phase-velocity maps (Section 3). Right-hand panel: the definition of the entire region (grey) and 4 subregions. The black dots on the map show the knots of the grid used in the phase-velocity tomography and indicate the area sampled by the inter-station paths. Left-hand panel: the phase-velocity anomalies with respect to the region average (top panel) and the absolute phase velocities in the subregions (bottom panel). Grey curve: the average of all the measurements in the data set.

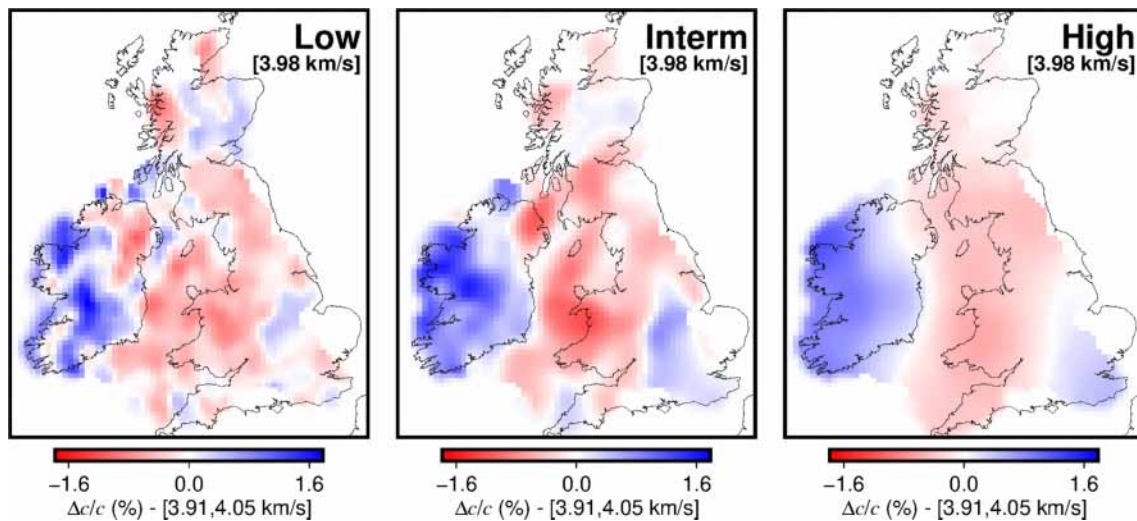


**Figure 8.** The effect of smoothing on the phase-velocity maps at 44 s period. A map that is not smooth enough (left-hand panel) fits noise in the data and is dominated by artefacts (noise). An overly smooth map (right-hand panel) is accurate, at its spatial wavelengths, but at a cost of a decrease in resolution. The intermediately smoothed map is preferable but, at close inspection, does not show an equally optimal regularization everywhere in the region (achieved, instead, in the composite, variable-regularization maps such as in Section 3).

entire set of station pairs, without any selection applied, we produce a density plot, as in the bottom panel in Fig. 6. Applying a loose selection on the data (such that for each measurement we only plot the curve closest to AK135 model in a certain period range, 20–50 s in this study) we can improve the density plot (top panel in Fig. 6) and obtain an average phase-velocity curve for the region that can then be used as the reference for

the final, more precise, one-by-one, phase-velocity measurements. The reference curve is obtained from the maximum values of the density distribution and then smoothed by means of a very weakly regularized inversion for a shear-velocity profile (Section 4.2).

Provided that a large number of measurements are contributing to the stack, one could analyse parts of the data for different subareas,

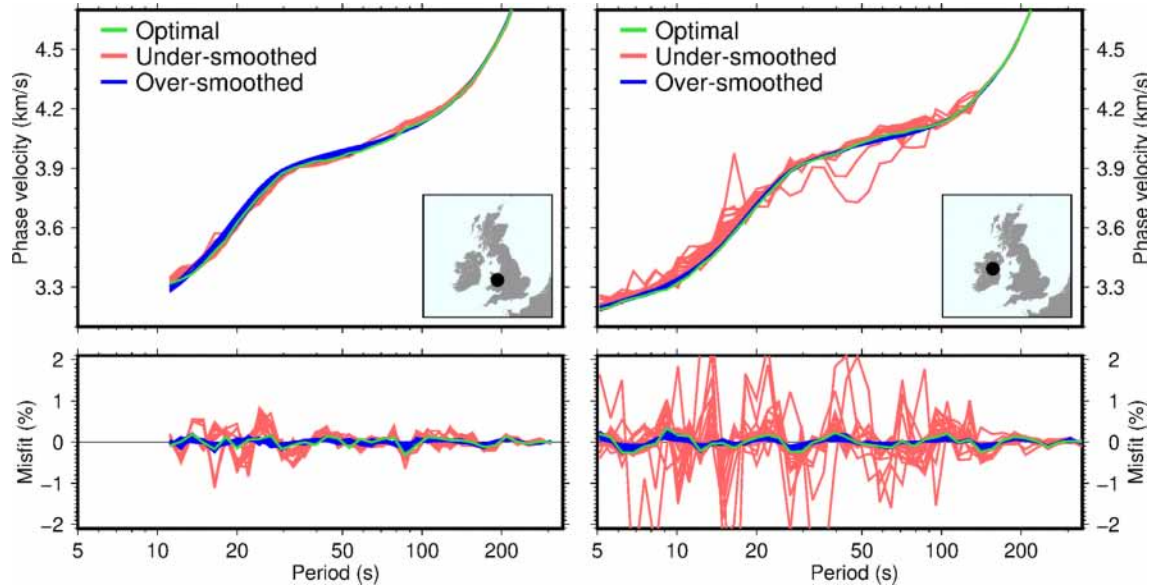


**Figure 9.** Selection of the optimal inversion smoothing for a point, based on the estimated errors of the phase-velocity curves yielded by phase-velocity maps. Top panel: phase-velocity curves at two points in Wales and in Ireland. The locations are mapped in the insets. The curves are extracted from phase-velocity maps with different levels of smoothness. Bottom panel: the period-dependent error of each phase-velocity curve. The error is estimated as the roughness of the phase-velocity curve, which we isolate by fitting it with a synthetic in a very weakly regularized inversion. Red lines: the curves obtained from rough maps. Blue lines: the curves obtained from smooth maps. Green line: the curve chosen as optimal.

obtaining different reference curves for them, in case the study area presents strong heterogeneity. In this study, we used five subareas, with average phase-velocity curves within them relatively similar to each other (Fig. 7). The average obtained from this stacking procedure is a useful reference for the measurements that follow but should not be taken as representing the real Earth structure, because systematic errors due to diffraction, scattered waves, the interference between the fundamental and higher modes and noise may bias the stack. Errors due to these effects are reduced by our strict measurement selection, described in Section 2.1. Although we obtained different reference curves for the five different subregions, the small differences between them did not justify using different reference curves in this study. Generally, one would use different reference curves if the study area comprises more diverse tectonic settings.

### 3 OPTIMAL RESOLUTION PHASE-VELOCITY MAPS

We wish to build a set of phase-velocity maps, at many periods within the range of the measurements, with an optimal resolving length at every point. The optimal resolving length is the smallest width of the averaging kernel such that the model error at the point is below a specified level (Backus & Gilbert 1968, 1970). The model error depends both on the data sampling and on the errors in the data and in the methods' approximations. According to the resolution-variance trade-off, the model error is expected to increase with the decreasing width of the averaging kernel (Backus & Gilbert 1970; Menke 2012).

The width of the averaging kernel at a point in our maps depends on the smoothing applied to the inversion: inversions with stronger smoothing produce models with broader averaging kernels. The optimal averaging kernel from the range given by the different levels

of smoothing can be selected if we can evaluate the model error at the point. Here we propose a method for estimating the errors of the sets of phase-velocity maps at every point. This amounts to tracking the errors to this key point of the tomographic scheme and provides a means to determine the optimal resolution at every point such that the effect of the errors is acceptably small.

#### 3.1 Phase-velocity maps with different smoothness

We invert phase-velocity curves from all inter-station pairs for phase-velocity maps using a least-squares technique, LSQR (Paige & Saunders 1987), with smoothing, which is the primary means of regularization, and weak norm damping (Lebedev & van der Hilst 2008; Deschamps *et al.* 2008; Darbyshire & Lebedev 2009; Pawlak *et al.* 2012). The maps are parametrized using a triangular grid with a 10 km knot spacing. The five model parameters at each grid knot include the isotropic-average anomaly and four anisotropic coefficients, two for  $\pi$ -periodic and two for  $\pi/2$ -periodic variations with azimuth (e.g. Smith & Dahlen 1973; Deschamps *et al.* 2008). The inversion at a period solves the system of equations yielded by all the path measurements at this period for the isotropic and anisotropic terms. Regularization is by means of norm damping (which penalizes model-parameter amplitudes), Laplacian smoothing (which penalizes the difference between the anomaly at a node and the average anomaly over this and the nearest neighbouring nodes), and gradient damping (which penalizes the differences between pairs of neighbouring model knots), all of which are applied independently to the isotropic and anisotropic components of the model (Lebedev & van der Hilst 2008; Endrun *et al.* 2008).

In the final, composite tomographic maps (Section 3) the solution at each of the 4328 grid knots comes from a whole-system inversion generally different from the one for the neighbouring points,

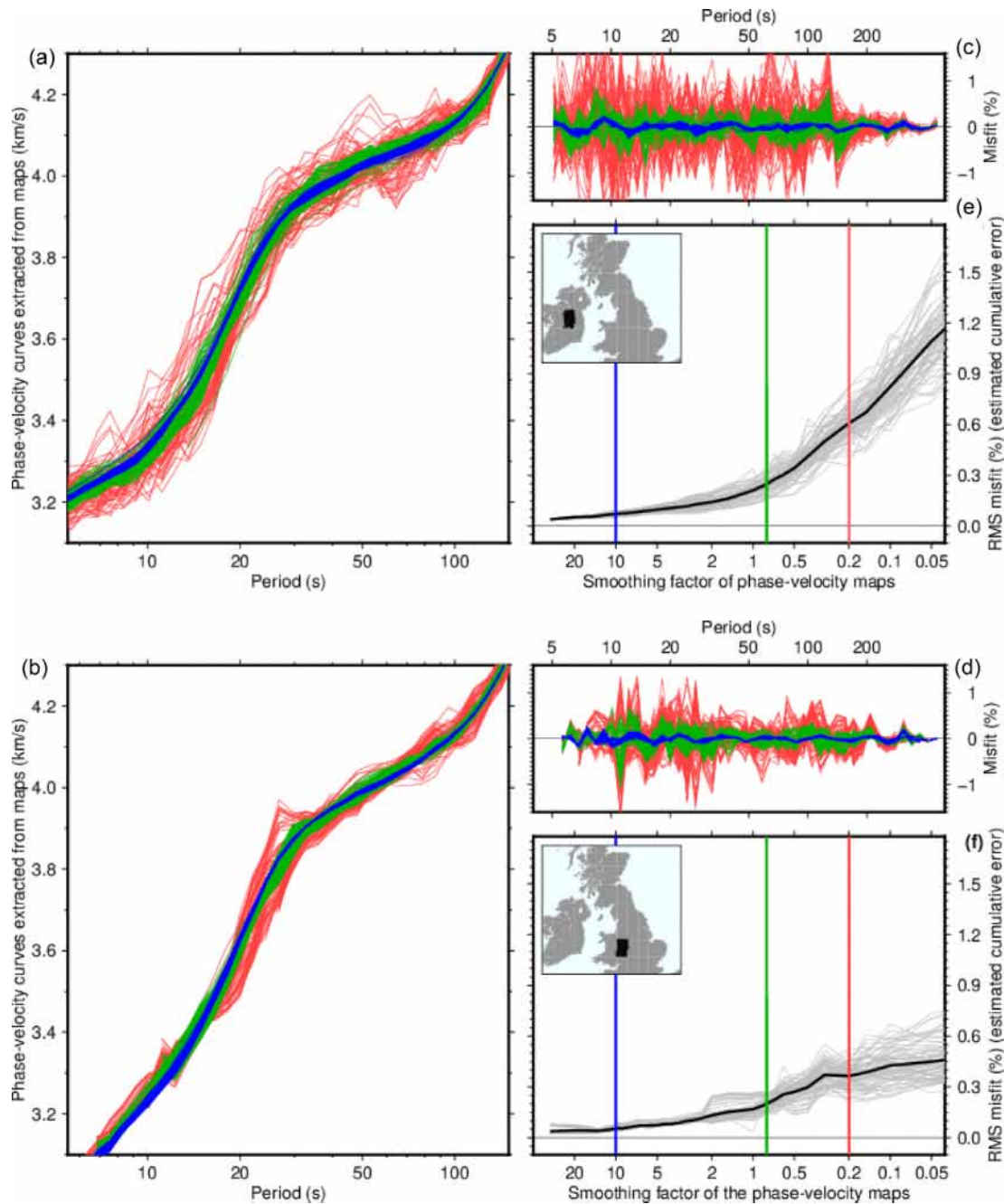


**Figure 10.** The decrease in the errors of phase-velocity curves with the increasing smoothness of the phase-velocity maps that they are derived from. The errors are estimated from the roughness of the phase-velocity curves. (a), (b): phase-velocity curves extracted from the phase-velocity maps computed with many different smoothing levels, grouped into rough (red), intermediate (green) and smooth (blue), at sets of neighbouring knots in Ireland and Britain (black dots in the maps). (c), (d): the misfits that quantify the period-dependent roughness of the curves and, by inference, their errors. (e), (f): the RMS misfit as a function of the smoothing applied (grey curves). Black: the average across the sets of neighbouring points.

with its own level of regularization chosen to yield an optimal local resolution. First, a series of 2-D inversions for phase-velocity maps is performed at each period, with the smoothing coefficients incremented at small steps from very low to very high. The gradual change in smoothing ( $S$ ) for the velocity maps (Fig. 8) is obtained with the Laplacian smoothing coefficient three times the gradient damping coefficient, norm damping as small as possible (chosen empirically so as to be able to suppress localized artefacts near the locations of some of the stations, for example, but

also to be small enough not to affect the amplitude of the anomalies elsewhere across the maps) and the regularization coefficients for the anisotropic terms 1.5 times those for the isotropic term. After an initial inversion, each phase-velocity map is recomputed with 25 per cent of the ‘outlier’ measurements discarded at each frequency (Lebedev & van der Hilst 2008). The outliers are defined here as the measurements fit the worst by the model; the procedure effectively selects the most mutually consistent measurements and removes the least mutually consistent ones, likely



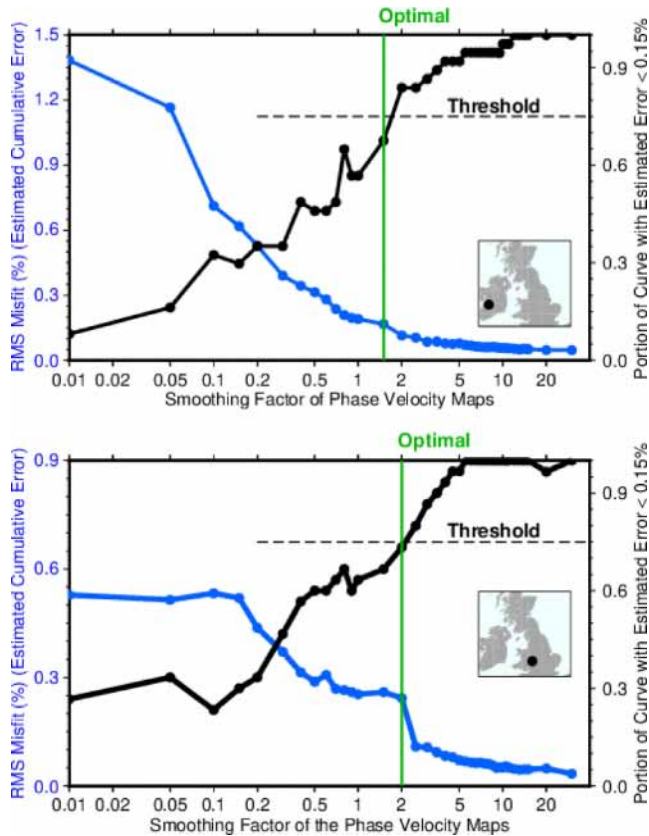


**Figure 11.** The cumulative error (RMS misfit) and the portion of the phase-velocity curve with the estimated error less than 0.15 per cent (our criterion for selecting the optimal regularization) change nearly monotonically with the smoothing factor of the phase-velocity maps that the curves are extracted from. The two examples are from grid knots in Ireland and Wales.

to contain the largest errors in the data set. Although this is effective in reducing noise in the data set (e.g. Lebedev & van der Hilst 2008; Schaeffer & Lebedev 2013; Celli *et al.* 2020), the remaining data still have errors, and it is these errors that translate into model errors and, together with the incompleteness of data sampling, impose lower limits on the optimal resolving lengths.

Once the 2-D tomographic maps are produced at each period (47 logarithmically spaced periods from 5.1 to 454.1 s) and for each smoothing level  $S_i = 0, 1, 2, \dots, 38$ , we extract phase-velocity curves at each of the 4328 knots of the grid (a total of 168 792 dispersion curves). The sample spacing is chosen to vary logarithmically with period so as to roughly balance the information contained within the different parts of the phase-velocity curve, sensitive to different depth intervals within the Earth (e.g. Lebedev *et al.* 2013). In the top panels of Fig. 9, we plot, as examples, the dispersion curves extracted at two knots of the grid, one in Wales (left-hand panel) and one in Ireland (right-hand panel).

### 3.2 Optimal smoothness at a point

As we show below, a local phase-velocity curve at a point—extracted from a set of phase-velocity maps at different periods—generally has errors that vary in concert with the roughness of the maps: the smoother the maps (the smaller the roughness), the

smaller the errors. This offers us a straightforward way of finding the optimal resolving length at a point: the averaging kernel width depends on the smoothing, and it is optimal when the estimated model error is just below a threshold. The problem is now reduced to finding the smallest level of smoothing of the maps such that the errors of the local dispersion curve are below the threshold. The procedure is repeated for each point. The optimal smoothness of the full inversion generally varies from one point to another.

To identify the optimal  $S_i$  for each knot of the model, we use the following strategy. For every local dispersion curve—for each  $S_i$  and at each knot—we estimate its errors by isolating its roughness. Due to the surface-wave sensitivity kernels' broad depth range and smooth variations with period, any realistic phase-velocity curve is smooth. This is true even for dispersion curves computed for unrealistic Earth models with highly oscillatory depth dependence of seismic velocities. The rough (not smooth) variations of phase velocities with period are, therefore, entirely due to errors. The frequency-dependent roughness of a phase-velocity curve can thus yield an estimate of its frequency-dependent errors (Ravenna *et al.* 2018).

The roughness of a phase-velocity curve can be isolated by means of a very weakly regularized inversion of it for a 1-D earth model. The smooth component of the curve can be matched closely by a synthetic curve computed for a best-fitting 1-D earth model (which is not required to be realistic in this inversion and can be oscillatory). The rough component is then given by the remaining misfit—varying rapidly with period—between the curve and its synthetic counterpart. This rough component cannot be fit by any Earth structure and is due to the errors of the dispersion curve. An estimate of the period-dependent error can now be obtained from the misfit or its envelope (Ravenna *et al.* 2018). This error estimate is conservative in the sense that the weakly regularized inversion fits the dispersion curve as closely as possible, even if this requires an unrealistic, oscillatory 1-D model. This may be offset, to some extent, by the fact that this approach will miss errors that do not vary with period or vary with period slowly and, thus, do not manifest themselves in the dispersion-curve roughness. Event mislocations, for example, could cause frequency-independent errors in source-station measurements, but they would not have a significant effect on inter-station measurements. In the inter-station measurements as used here, an instrument-response error at one of the two stations could produce a measurement error with a weak frequency dependence, but this would be likely identified by our routine comparisons of the measurements using sources in the two different directions from the station pair. For any remaining errors in the data to translate into frequency-independent errors in the phase-velocity curves, they would need to cause the same bias in the phase-velocity maps in the same location at different periods. The largest source of remaining errors is probably unmodelled surface-wave diffraction. Fortunately for our purposes here, it is strongly frequency-dependent (e.g. Meier *et al.* 2004; Kolínský *et al.* 2021), which is manifest in the curve roughness. For these reasons, the frequency-independent errors are likely to be small.

Our weakly regularized inversion for a 1-D shear velocity profile is a non-linear, Levenberg–Marquardt gradient search (e.g. Meier *et al.* 2004; Lebedev *et al.* 2006; Endrun *et al.* 2008; Erduran *et al.* 2008; Agius & Lebedev 2013, 2014, see Section 4 for details on the inversion algorithm). The misfit is computed as the relative data-synthetic misfit integrated along the length of the curves. With all the 1-D inversions performed using the same weak regularization, we find that the relative data-synthetic misfit is smaller for curves extracted from maps with higher  $S_i$ , and higher for curves

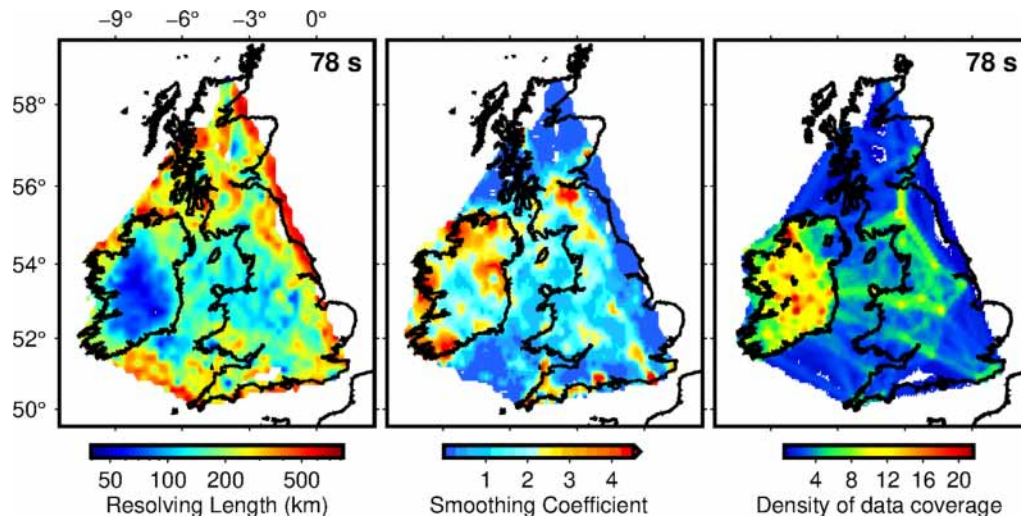


**Figure 12.** Left-hand panel: the laterally varying resolving length yielded by the optimal-resolution tomography. A 78-s phase-velocity map is plotted as an example. The resolving length and the parameter value at each point were determined in a series of inversions of the entire system. The optimal width of the averaging kernel—defined as the smallest averaging kernel width such that the error is below a threshold—was found by varying it in a broad range, using varying smoothing parameters. Middle panel: laterally varying smoothing coefficients determined and applied in the course of the optimal-resolution tomography. Phase-velocity maps at all periods are computed with these smoothing coefficients. Note that the smoothing coefficient value does not scale with the smoothness or the resolving length. Right-hand panel: the density of the data coverage at 78 s, computed as the sums of the columns of the sensitivity matrix, determined by the path coverage.

extracted from maps with lower  $S_i$  (Fig. 9). These inversions are not meaningful in terms of real Earth structure; we use them only to isolate the roughness of the curves, which is entirely due to errors.

Extremely smooth phase-velocity maps are the most robust and accurate, at their spatial wavelengths, but at the cost of lower resolution: they display large-scale structural trends but fail to show structure at a high level of detail. Conversely, phase-velocity maps that are not smooth enough will fit noise and may be dominated by artefacts.

Figs 10, 11 and A1 show that the error of the phase-velocity curves, estimated by the roughness-isolating 1-D inversions, decreases with increasing smoothing of the 2-D velocity map. Fig. 10 shows the root mean square (RMS) misfit (panels e and f) computed for every inversion at two different sets of knots, in Ireland (top panel) and in Britain (bottom panel), as indicated by the black dots in the maps. Panels (a) and (b) show the phase-velocity curves extracted from the 2-D tomographic maps with three different level of smoothing ( $S$ ), as indicated by the colours (red, green and blue, respectively for ‘low’, ‘intermediate’ and ‘high’  $S$ ). The relative misfit is shown in panels (c) and (d). It is clear from this figure that the smoother the 2-D phase-velocity map, the smaller the misfit in the 1-D inversion for shear velocity. Importantly, the estimated error increases nearly monotonically with the decrease of the smoothing coefficient, which also confirms that the models converge consistently, unaffected by any local minima, for example. The same behaviour is observed in Fig. A1, where the portion of the phase-velocity curves with estimated errors less than 0.15 per cent, rather than the RMS misfit, is plotted as a function of  $S$ .

The data sampling given by our large phase-velocity data set is so redundant that random noise largely cancels out, but not the systematic errors, which may be due to wave propagation effects and instrumental problems. This is apparent from the fact that the

error of the local phase-velocity curve does not scale with the data sampling (Fig. 12, Section 3.3).

We now define an empirical criterion to identify the optimal  $S_i$  for each knot of the model. We set a threshold of 0.15 per cent for the relative misfit and accept only those phase-velocity curves that produce misfit within this threshold at at least 75 per cent of the periods. This way, curves too rough (low  $S_i$ ) are discarded, and we can select the roughest of the remaining, smoother curves as the optimal one, with the corresponding optimal level of smoothing and the corresponding optimal averaging kernel. The criteria for choosing the error threshold have been chosen empirically after extensive testing.

In Fig. 13, the composite phase-velocity maps constructed using our preferred threshold for the acceptable errors of the local dispersion curves (c) are compared with two composite maps produced with higher thresholds and two composite maps with lower thresholds—that is, two looser and two stricter selections (columns (a), (b) and (d), (e) respectively)—for three different periods. Our empirical threshold choice is intended to yield an estimate of an optimal resolving length at every knot. In Fig. 11 we show that the cumulative error, as well as the portion of the curve with estimated error less than 0.15 per cent, are changing with  $S$  nearly monotonically. Parts of the maps near the region boundary, where the coverage is extremely low, have been removed from the analysis based on sensitivity-matrix column sums—accepting only the knots with the sum’s value over a certain threshold.

The map of the optimal resolving length at 78 s period is shown in Fig. 12, together with a map of the chosen values of  $S_i$  and a map of the density of the data coverage. The optimal resolving length does not scale with the density of data sampling. This is, in part, due to the complex azimuthal unevenness of the coverage and, in part, due to the errors in the data—given the substantial



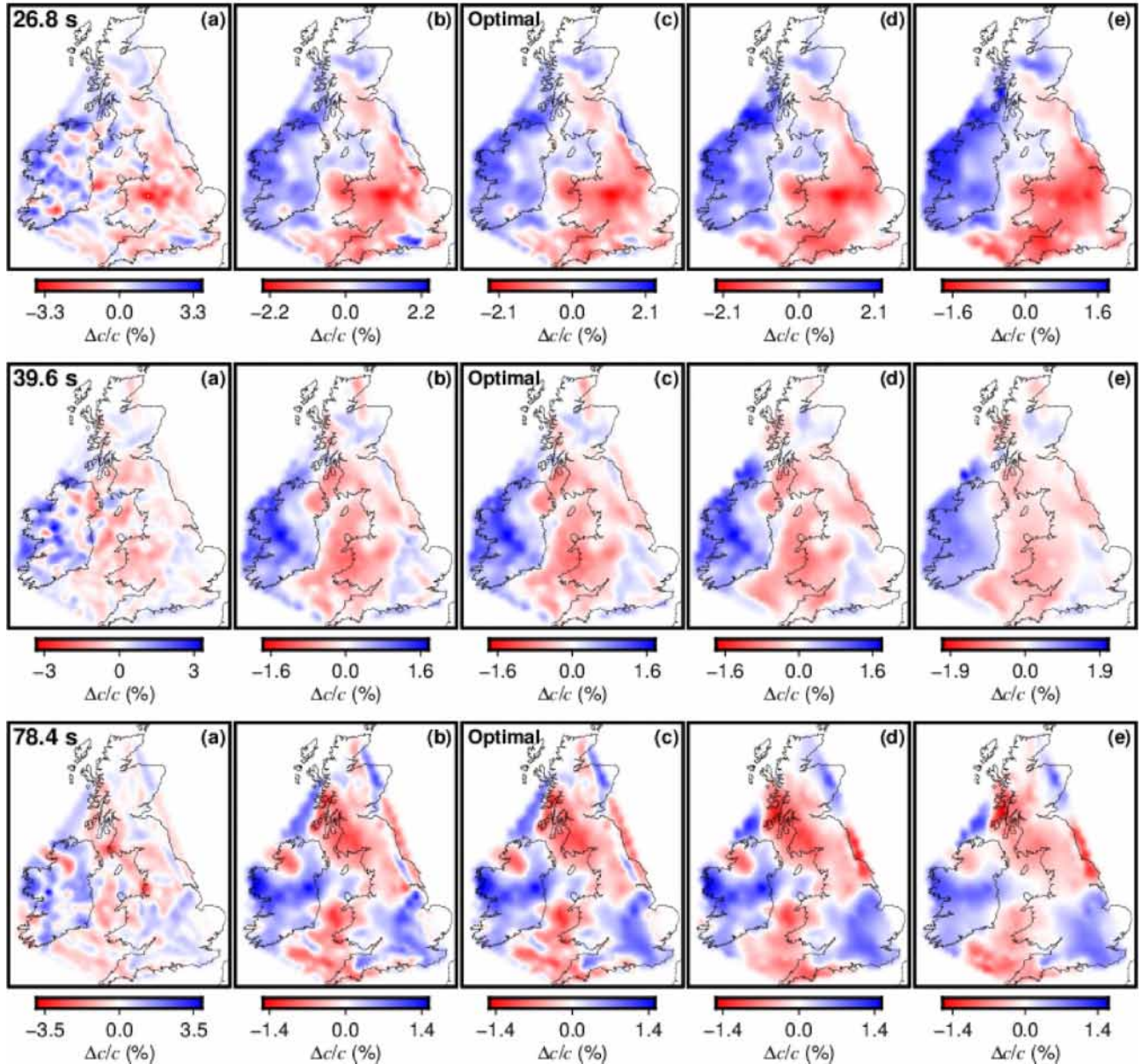


**Figure 13.** Composite, variable-resolution, phase-velocity maps constructed using different thresholds for acceptable errors of the local dispersion curves. In panel (c) we show the velocity maps with optimal resolution, the maps in (a), (b) and (d), (e) correspond to looser and stricter criteria of selection, respectively, with regard to the error threshold.

redundancy of the data set, probably due to systematic errors primarily. The optimal values of the smoothing coefficient also do not scale with the data sampling and could not be estimated directly from the column sums of the sensitivity matrix. This necessitates the sequence of numerous inversions included in our approach.

### 3.3 Estimating spatial resolution

The procedure used to estimate the resolution length at a point is as follows. We simulate a spike perturbation for this one knot of the model grid, with no anomaly elsewhere, and use our sensitivity matrix  $\mathbf{A}$  to determine the synthetic data vector  $\mathbf{d}$  (eq. 1). We

then solve the inverse problem with exactly the same regularization as applied to the inversion of the data (Fig. 14) and evaluate how much the delta-like perturbation has spread after the inversion. To do so, we register the values of the output anomaly along great circles that extend  $4^\circ$  from the point in each direction and are oriented at densely spaced azimuths covering the full azimuth range (Fig. 15). Smooth curves through the points, determined using cubic splines, display a natural bell shape (Fig. 15, left-hand panel), similar to a Gaussian function. The half-width of the averaging kernel is computed as an average over the half-widths at the half-maxima (HWHM) of the curves at all azimuths. The resolving length is twice that, that is, the full width at the half maximum.



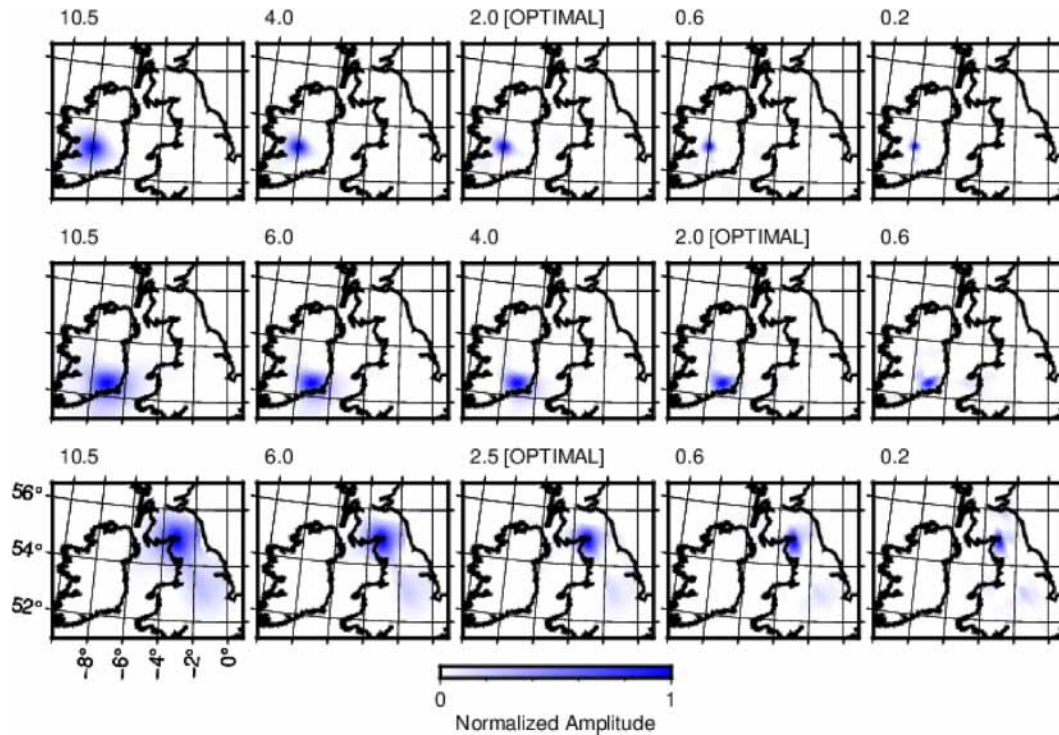


**Figure 14.** Point-spread functions at three different locations, two in Ireland and one in Scotland, yielded by differently smoothed tomographic test inversions. The smoothing coefficient  $S$  is indicated at the top left of each plot.

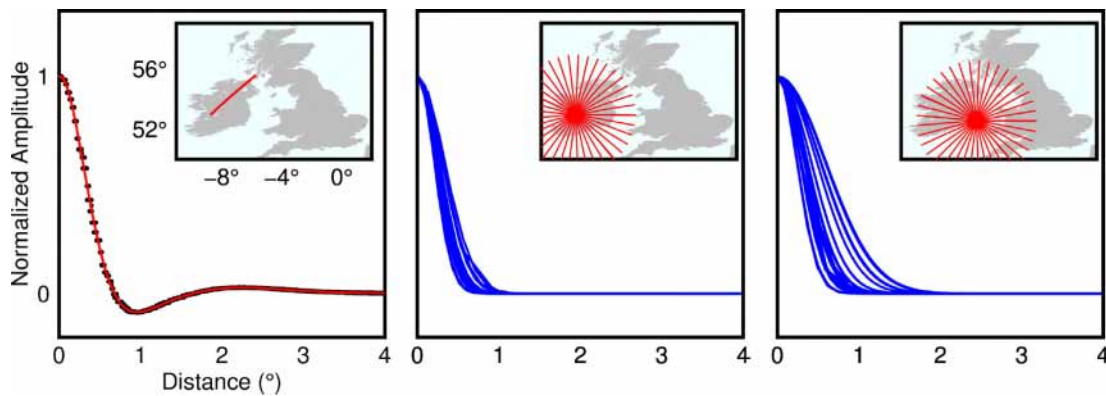


**Figure 15.** Estimation of the averaging kernel and resolving length. Left-hand panel: an estimate of the averaging kernel at a point along one azimuth through the point. Anomaly values at grid points along the line shown on the map are matched closely by a bell curve, computed using cubic splines so as to fit the points. Centre, right-hand panel: illustration of different resolving length for two different locations, given by theoretical Gaussian functions computed from the measured half width at half maximum along the full range of densely spaced azimuths. The resolving length is determined as the average of the full width at half maximum given by the curves at the different azimuths.

The procedure is repeated for every knot of the grid and for every smoothing level. The method for resolving-length estimation can break at the edge of the region, where the data sampling deteriorates. Where the HWHM cannot be defined (e.g. the amplitude of the anomaly is too low, or its width too high), the resolving length is set to infinite. Maps of the estimated resolving length at different periods obtained with this method are shown in Fig. 16.

The optimal-resolution phase-velocity maps, for a selection of periods, are shown in Figs 17 and 18. It is not possible to identify the errors in the measurements going into the tomographic inversion, but we can evaluate them between the phase-velocity map step and

the 1-D inversion step, at which point the optimal resolution is determined. The estimated optimal resolution shows smooth lateral variations, confirming the robustness of the procedure (Fig. 16).

Fig. 19 illustrates the advantages of using the optimal resolution scheme (1st column) compared to inversions with a constant smoothing factor (2nd, 3rd and 4th columns). Using a uniform (rough, medium or smooth) regularization, we either lose details (if the model is too smooth) or introduce artefacts (if the model is too rough), or both, in different parts of the model. The optimal resolution scheme allows us, instead, to optimize the amount of the structural information extracted from the data while keeping estimated model errors below a consistent threshold.

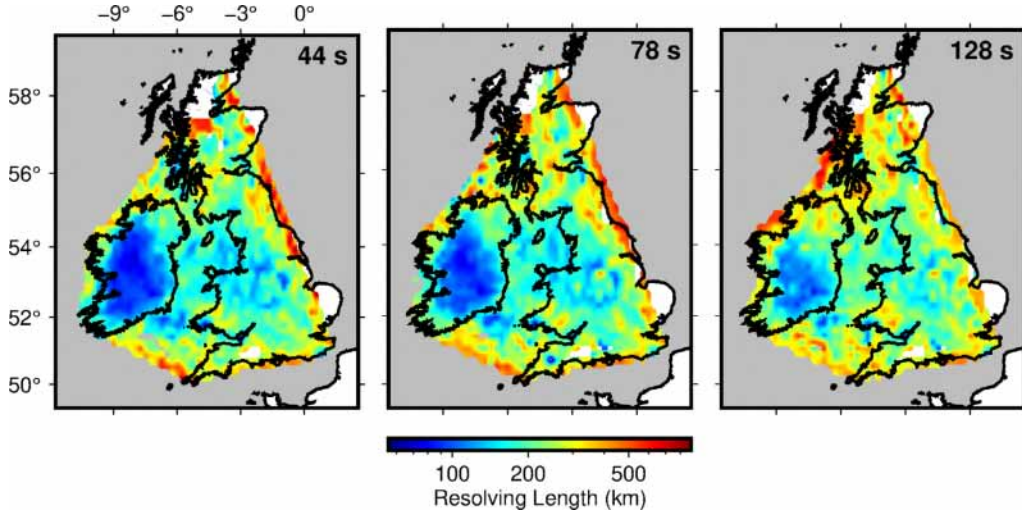


**Figure 16.** The resolving length of the optimal model is similar at different periods, fulfilling an important condition for the accuracy of the procedure.

#### 4 INVERSION FOR SHEAR VELOCITY STRUCTURE

The optimal-resolution phase-velocity maps are now inverted, point by point at each knot of the model grid, for 1-D, shear-velocity profiles. These profiles are then combined to form a 3-D model of the crust and upper mantle. The regularization of these 1-D inversions is the same at every knot.

##### 4.1 Removal of noisy tails of local dispersion curves

Before proceeding with the 1-D inversion of the local, phase-velocity curves for shear-velocity structure, we apply additional quality checks to the dispersion curves. Even though the local curves are largely smooth, by construction, some of them have noisy ‘tails’—usually, the shortest-period portion of the curve having more noise than the rest of it (Fig. 20). The noisy tails are identified by evaluating the relative misfit for the edge portions of each dispersion curve (8 points for the shorter periods and 3 for the longer periods); this misfit, calculated as in Section 3 using a weakly regularized inversion, quantifies the roughness and, by inference, the error of the curve. If the misfit at any point within the tail exceeds an empirical threshold of 1.6 times the standard deviation over the full period range of the curve, then the entire tail is removed.

##### 4.2 Gradient-search inversions

Ravenna & Lebedev (2018) showed that a well-tuned, non-linear, gradient-search inversion of phase-velocity curves yields robust 1-D Earth models nearly indistinguishable from the median model given by a Bayesian, MCMC inversion scheme. While a Bayesian approach still has advantages in providing a *posteriori* model uncertainties, we opted for a non-linear gradient-search technique, as the data set size would have made probabilistic inversions prohibitively expensive. We do, however, perform a series of gradient inversions in each case, using variable regularization to sample the model uncertainty at different depths.

We use the same non-linear, Levenberg–Marquardt gradient search inversion algorithm that we used to isolate the noise in Section 3, with the difference that the inversions are not regularized too weakly. We choose regularization in the form of norm damping on each depth parameter, sufficient to penalize and exclude unrealistic, oscillatory  $V_S$  models. Fig. 21 illustrates how the  $V_S$  profiles with insufficient regularization (left-hand panel) provide a marginally better misfit than sufficiently regularized ones (right-hand panel) but are oscillatory and likely to be fitting the noise.

The algorithm computes synthetic phase velocities at each iteration directly from  $V_S$ , compressional velocity ( $V_P$ ), density and attenuation using the forward solver MINEOS (Masters *et al.* 2007), adapted for the travelling wave decomposition (Nolet 2008) and streamlined for speed (Lebedev *et al.* 2013; Ravenna & Lebedev 2018). The depth-dependent ratio between  $V_S$  and  $V_P$  is kept fixed during the inversion, equal to the values in the reference model. Density and the compressional and shear attenuation factors are fixed at the reference values, taken from PREM (Dziewonski & Anderson 1981) and AK135 (Kennett *et al.* 1995), respectively. The perturbations in the model, from the surface to the shallow lower mantle ( $\sim 1300$  km), are controlled using 13 triangular-shaped basis functions in the mantle and 3 boxcar-shaped ones in the crust (e.g. Bartzsch *et al.* 2011; Agius & Lebedev 2013). The triangular basis functions are defined by linear interpolation between neighbouring depth knots; the boxcar ones represent constant-velocity layers. The depth of the Moho and two intracrustal discontinuities are additional inversion parameters.

##### 4.3 Reference model

We used a three-layered reference crustal model of the region based on CRUST 2.0 (Bassin *et al.* 2000) and previous studies in the area (Landes *et al.* 2000; Tomlinson *et al.* 2006; Davis *et al.* 2012; Licciardi *et al.* 2014), with a reference Moho depth of 30 km. The reference model for the mantle is a modified version of AK135 (Kennett *et al.* 1995), recomputed at 50 s and characterized by constant shear velocities ( $4.45 \text{ km s}^{-1}$ ) from the Moho



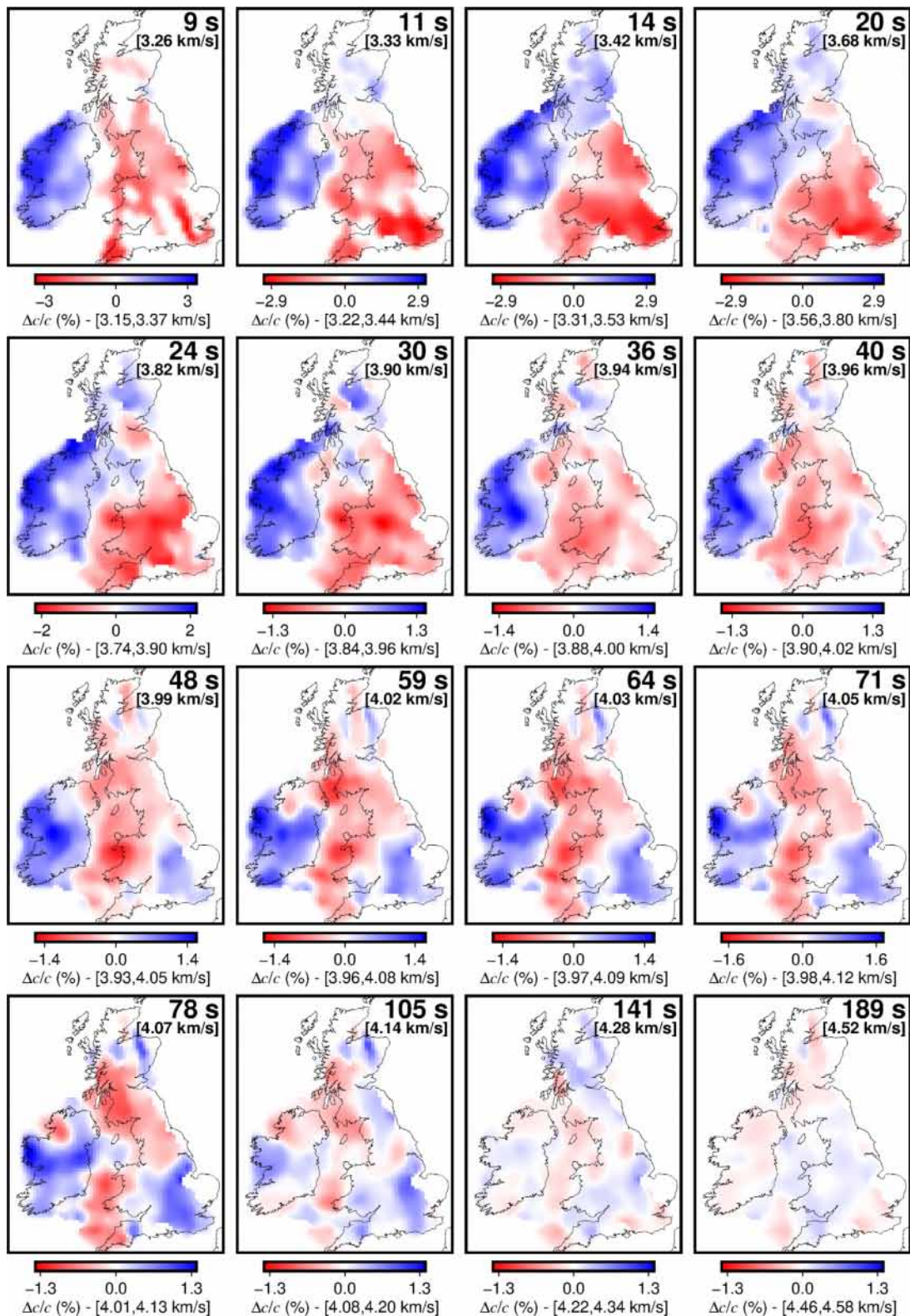


**Figure 17.** Optimal resolution phase-velocity maps of the region. The phase-velocity anomalies are with respect to the region average, indicated in the top right corner of each frame. The minimum and maximum phase velocity is given below each colour scale. Parts of the maps where the coverage is extremely low (for example, at the edges of the region, where the coverage deteriorates and the data sampling is insufficient to constrain the structure) have been removed from the analysis, based on sensitivity-matrix column sums-accepting only knots with values over a threshold.



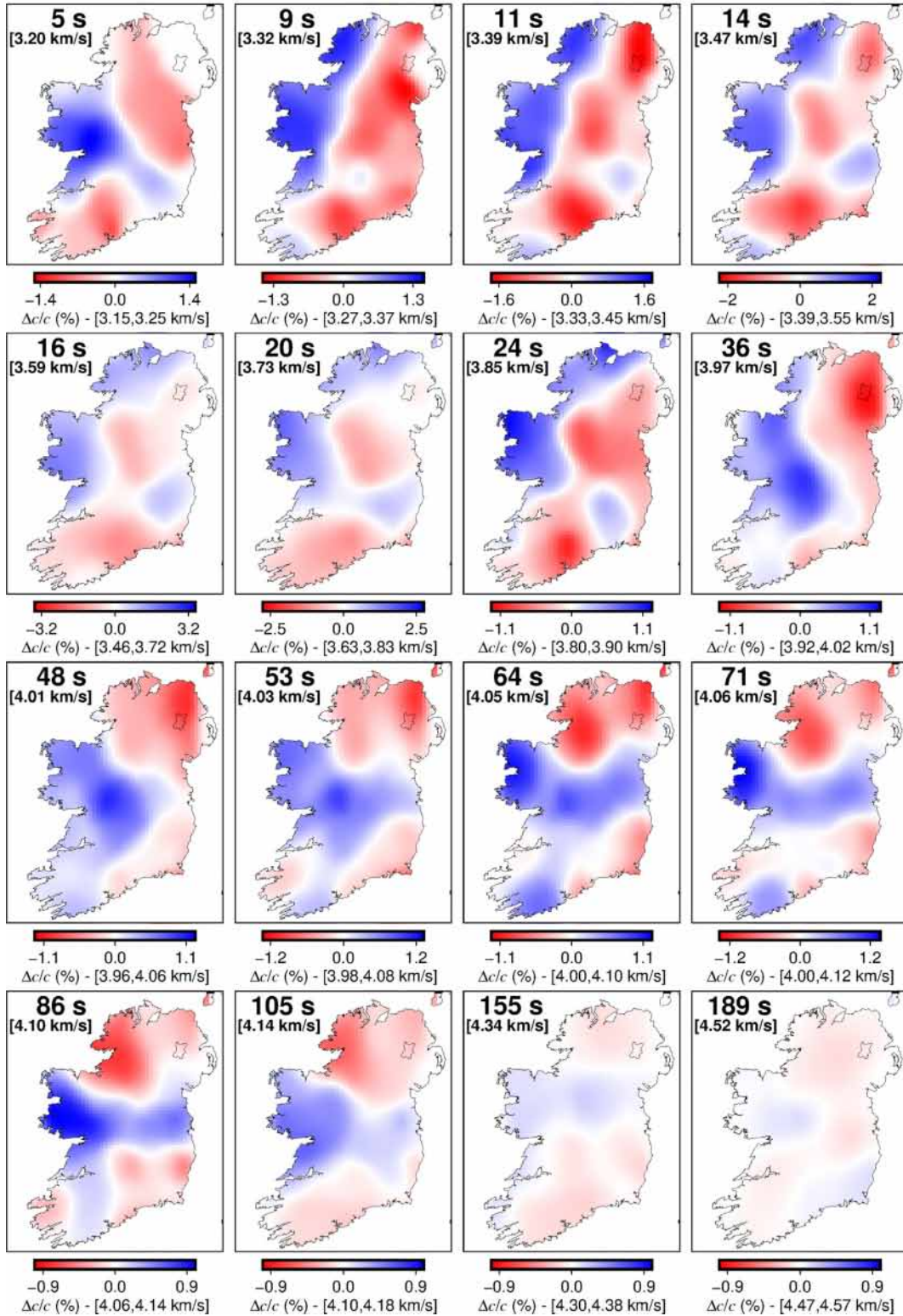


**Figure 18.** Optimal resolution, phase-velocity maps of Ireland. The phase-velocity anomalies are with respect to the Ireland average, indicated in the top left corner of each frame. The minimum and maximum phase velocity is given below each colour scale.

down to 190 km depth and linearly increasing shear velocities below. The reference period of the  $V_S$  model is 50 s, approximately in the middle of the period range of the data, in the logarithmic sense. This minimizes errors from unknown variations in

the attenuation structure of the mantle (Lebedev & van der Hilst 2008). The density for the reference model was taken from PREM (Dziewonski & Anderson 1981), as AK135 presents a questionable sharp density increase with radius in the uppermost mantle.

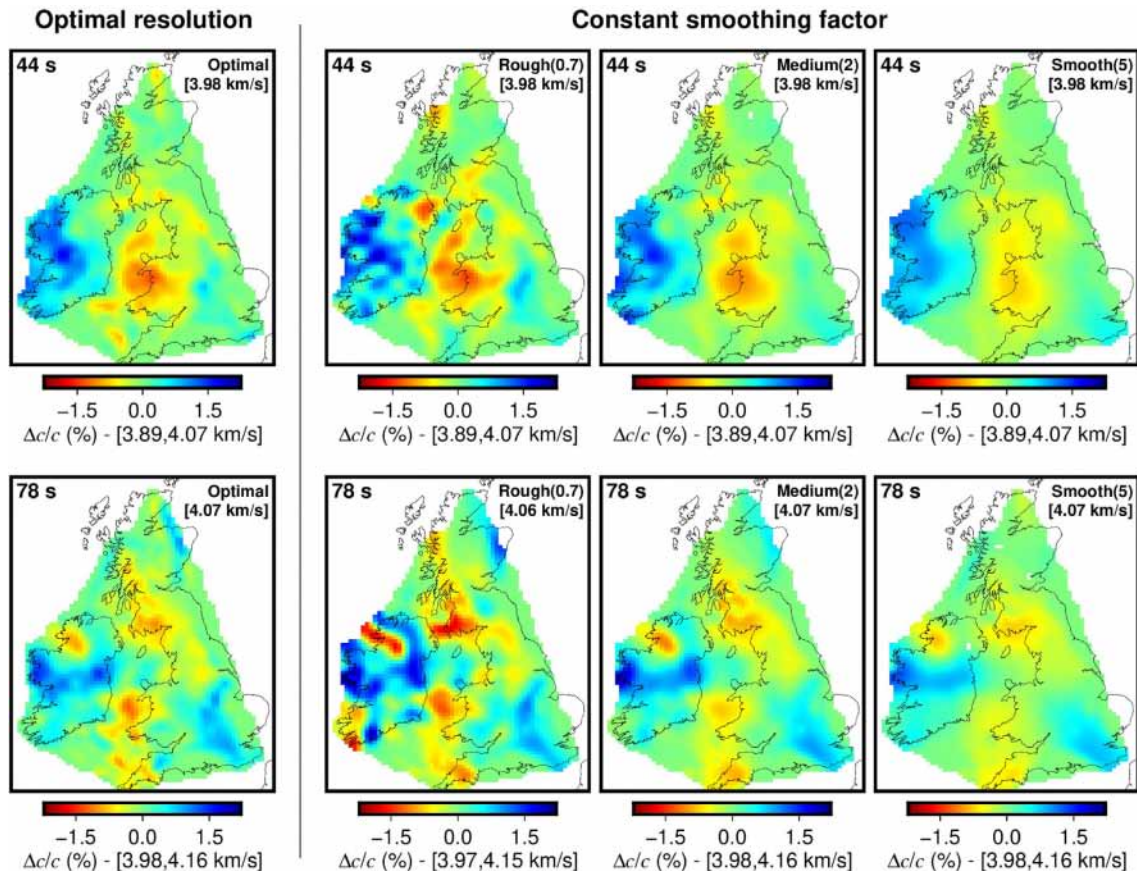


**Figure 19.** Optimal resolution maps (left-hand column) at two periods (44 s, 78 s) compared with constant-smoothing-factor maps computed using different levels of smoothing (second to fourth columns). The composite, optimal resolution maps display lateral variations in resolution as warranted by the data coverage and errors.

We performed extensive tests, however, and established that this modification does not substantially change our results. The reference model is plotted in Figs 21 and 22 with a dashed black line.

#### 4.4 Regularization of the inversion

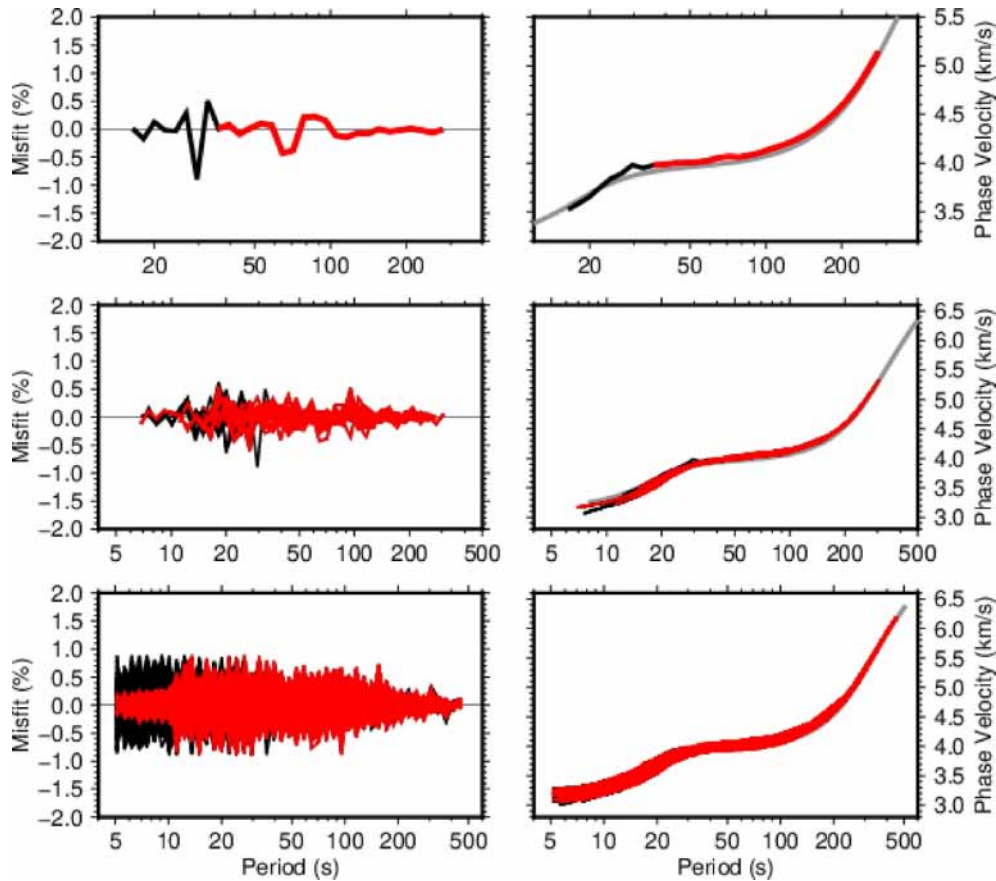
Suitable regularization of the inversion for  $V_S$  profiles was determined in a series of tests. The regularization is by means of norm damping on the inversion parameters and is the same at all the grid knots. Instead of one inversion per location, we performed a series of 900 inversions at each point that produced a bundle of possible models, all fitting the data approximately equally well. The relative damping for each basis function is allowed to vary randomly within a range of values. This produces a set of 50 models for each knot at each damping level ( $d_j = 0, 1, 2, \dots, 49$ ) as, for example, in each of the panels in the middle row in Fig. 21. A global damping factor, constant for all basis function, then multiplies the relative factors in each inversion ( $D \times d_j = 0, 1, 2, \dots, 49$ , with  $D = 1, 2, 3, \dots, 18$ ). The relative damping  $d_j$  is randomly changed at different depths (each basis function has a different value of  $d_j$ ) in order to minimize the potential bias due to a subjective choice of regularization. The overall damping factor ( $D$ ) is used to obtain differently regularized bundles of models.

Fig. 21 shows 4 differently damped ( $D$ ) sets of models, with each set including 50 models with randomly varying relative damping ( $d_j$ ). In order to cover a wide range of potentially suitable regularization parameters, 18 differently damped (varying  $D$ ) models were computed that produced  $4328 \times 50 \times 18$  independent, non-linear, gradient-search inversions. This allowed us to identify an optimal damping strength ( $D$ ) for our final shear velocity model. We note that the optimal damping strength for the shear-velocity inversion is equal at every knot of the grid and does not vary as in the composite, phase-velocity maps (Section 3).

#### 4.5 $V_S$ model construction

In Fig. 22, we show sets of inversions at five different locations for a defined choice of damping factor  $D$ . The optimal damping factor is chosen according to the following criteria. We do not wish to introduce unnecessary complexity in our model by overfitting the data; if a simpler model fits the data equally well (according to the general principle of parsimony, also known as Occam's razor (e.g. Constable *et al.* 1987; Bodin *et al.* 2016)) then we choose this over a more complex model.

The accepted  $V_S$  profiles are then resampled at a 0.1 km step, and the final  $V_S$  maps are constructed, for each global-damping level. The 1-D profile at a point is computed as an average over the bundle of the 50 models obtained at this knot. Maps of our final



**Figure 20.** Removal of the ‘noisy tails’ of the phase-velocity curves prior to the point-by-point, 1-D inversions for shear-wave velocity structure. The original curve is shown in black, the curve after the removal of the noisy part is shown in red. The phase-velocity curves are shown in the right-hand column, and the period-dependent error estimates (the relative misfits) given by weakly regularized inversions of the curves—in the left-hand column. Top panel: an example of one phase-velocity curve only. Middle panel: 30 curves randomly selected from the entire data set. Bottom panel: 5000 randomly selected dispersion curves.

velocity model are plotted in Figs 23 and A2. A comparison of the shear velocity maps computed with different damping levels is in Fig. A3, where we show how, for a reasonable choice of damping, the maps exhibit similar features, although the amplitudes are not preserved. 1-D inversions with stronger damping consistently produce smoother 3-D models.

#### 4.6 3-D shear velocity structure beneath Ireland and Britain

Figs 23 and 24 show the *S*-wave velocity structure of the crust and upper mantle beneath Ireland and Britain and the map of the Moho depth, resolved by our tomography. The Moho map constrained by our surface-wave inversion (Fig. 24) shows general agreement with published results from wide-angle profiles and receiver functions (e.g. Landes *et al.* 2007; Kelly *et al.* 2007; Davis *et al.* 2012; Licciardi *et al.* 2014). Our results and the ones obtained by Licciardi *et al.* (2014) using teleseismic *P*-wave receiver functions both display a thinning of the crust from SW to NE in Ireland, but also present some differences. Constrained by more data, our Moho depth map is less smooth than that of Licciardi *et al.* (2014). The broad agreement of our results on the topography of the Moho with published independent evidence confirms that the  $V_S$  distributions in our models are not biased substantially by trade-offs with the crustal thickness.

The *S*-wave velocity model (Fig. 23) offers important new insights into the structure and evolution of the Ireland–Britain region. A robust, low-velocity anomaly beneath the Irish Sea and its surroundings persists in the models from  $\sim 50$  to at least 140 km depth, indicating an anomalously thin lithosphere, underlain by warm asthenosphere. The model represents a substantial addition to the geophysical evidence on the lithospheric structure and evolution of the Ireland–Britain region.

## 5 DISCUSSION

### 5.1 Optimal resolution tomography

Our optimal resolution tomography is developed to solve the problem as posed by Backus & Gilbert (1970): it determines localized averages over optimal resolving lengths at every point. The optimal resolving (averaging) lengths are the shortest such that the model error is below a specified level. The averaging length is a function of the global smoothing of the model, with the optimal level chosen using many inversions with different smoothing strengths. The key element of the method is the direct evaluation of the posterior model error of the phase velocity maps, which can come from both random and systematic errors in the data, as well as



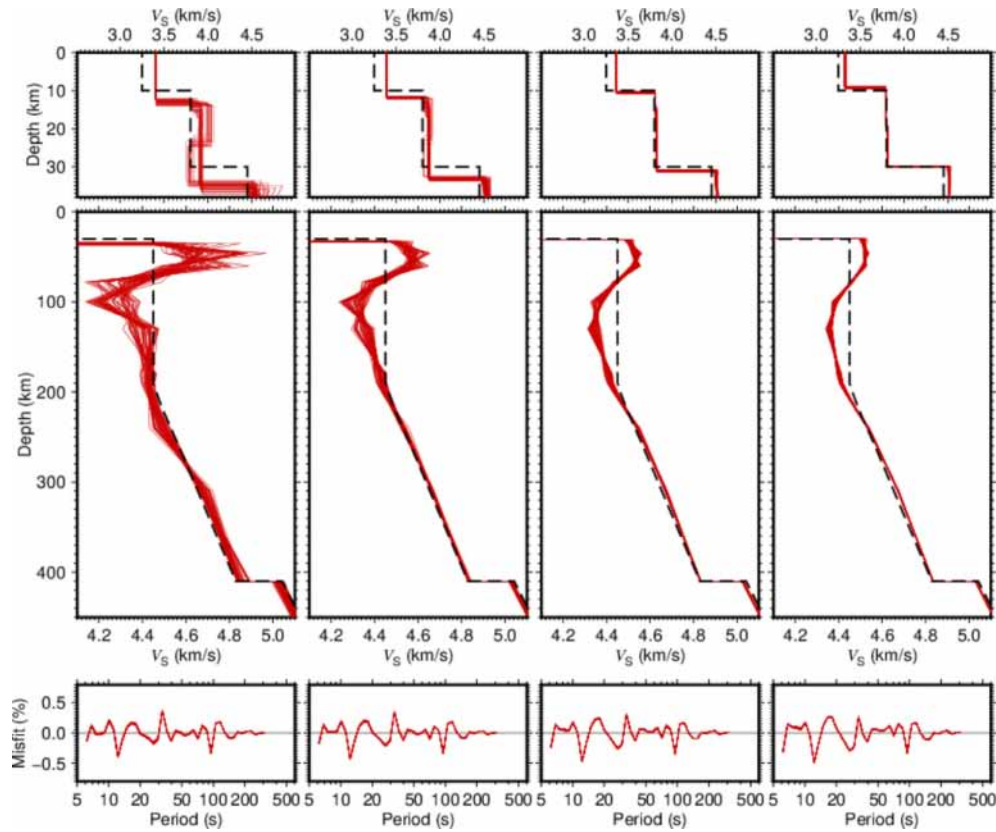


**Figure 21.** Inversions of the local phase-velocity curve at one grid knot (54.93N, 7.9W) for  $V_S$  profiles, with increasing damping from left to right-hand panels. The reference model is plotted with a dashed black line. Top panels: a zoom on the crust; middle: the profile from 0 to 450 km; bottom panels: the phase-velocity misfit. The models yielded by the inversions are non-unique but the robust features in the  $V_S$  profile are evident.

from the incompleteness of data sampling. In other words, the optimal resolution is chosen as the highest achievable subject to the errors.

Importantly, the estimated error decreases monotonically with the increasing smoothing of the 2-D tomographic maps. This allows us to use a threshold on the errors to determine the optimal resolution. Optimal resolution does not scale with the density of the data coverage: due to systematic data errors, some of the best-sampled locations display relatively low lateral resolution. At long periods, the resolution is generally lower due to the greater wavelengths of the waves but, typically, so is the sampled deep heterogeneity, which mitigates the negative effect of the resolution decrease with increasing period. We observe that the resolution of the maps (Fig. 16) at different periods is similar, confirming the stability of our method in terms of the weak dependence of the resolving lengths on the period of the phase-velocity maps. In view of the very high heterogeneity of seismometers' distribution on the Earth's surface and the persistent and ubiquitous systematic errors in the seismic data, the new, optimal resolution tomography method can benefit studies in many regions and at different scales.

## 5.2 Lithospheric heterogeneity

Our tomography reveals substantial, previously unknown lithospheric heterogeneity in the area, offering exciting new insights

into the structure and evolution of the Ireland–Britain region. Constrained by abundant, newly available data, our model demonstrates that the assumption of a constant lithospheric thickness across Britain and Ireland, used in the past, is not valid. At the upper-crustal depths, Ireland and Scotland exhibit similar seismic velocities, both showing clear boundaries between low-velocity sediments in basins and the high-velocity crystalline crust elsewhere, as one would expect from the continuity of the geological terrane boundaries across the Irish Sea. These contrasts are already evident in the phase-velocity maps, for example at 14 s (Fig. 17). In the deeper crust and lithospheric mantle, most of Ireland is surprisingly different from Scotland, showing substantially higher velocities. Our phase-velocity maps over the Irish landmass are in agreement with the earlier results from Polat *et al.* (2012) but provide much greater regional detail. Both studies show high velocities in the north-western and lower velocities in the eastern part of the island. Our model also shows good agreement with the results of active seismic surveys (e.g. Landes *et al.* 2005), including on the Moho depth (Section 5.3).

The thinning of the lithosphere beneath the circum-Irish Sea region, evident from the model (e.g. Figs 17 and 23), matches the area of the Paleogene uplift and volcanism and offers important evidence on their mechanisms. The high velocity anomaly in west-central and east-central Ireland reveals a surprisingly thick lithosphere and may indicate the incorporation of previously unknown Precambrian continental blocks into the Irish landmass during the Caledonian Orogeny. This interpretation is consistent with the observations of

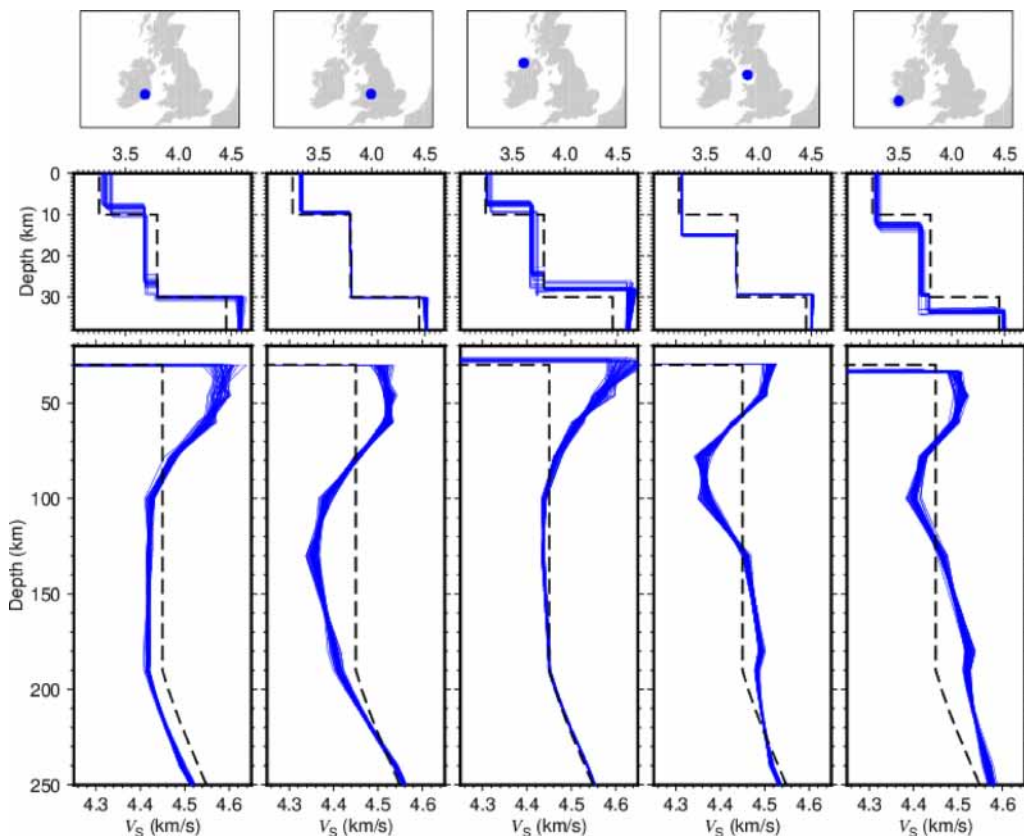


Figure 22.  $V_S$  profiles at five selected locations in Ireland and Britain.

Precambrian rocks in the north and west of Ireland (Chew & Stillman 2009). Detailed investigation of these features in the context of the available geological evidence will be the subject of forthcoming publications.

### 5.3 The Moho depth

The large-scale variations of the Moho depth across the region are generally consistent across different recent studies (Landes *et al.* 2005; Tomlinson *et al.* 2006; Kelly *et al.* 2007; Davis *et al.* 2012; Licciardi *et al.* 2014, 2020). Ireland and Britain generally show thicker crust (32–35 km) in Avalonia, south of the Iapetus Suture Zone (ISZ, Fig. 23), and thinner crust north of the ISZ, down to as thin as 26 km in northwest Scotland and Ireland. Davis *et al.* (2012) estimated Moho map for several profiles using receiver functions and found that the crustal thickness across Ireland and Britain varies between 24 and 36 km, with thicker crust beneath north Wales and central Scotland and thinner crust beneath northwest Scotland and northwest Ireland. Landes *et al.* (2005) used data from 11 seismic refraction profiles onshore and offshore to investigate the crustal velocity structure of Ireland and surrounding seas and reported a crustal thickness varying from 28.5 to 32 km in Ireland. Kelly *et al.* (2007) compiled a regional model for crustal seismic  $P$ -wave velocities for NW Europe, from wide-angle reflection and refraction profiles and found, for Britain and Ireland, Moho depths similar to existing crustal thickness maps, including estimates of the uncertainties for the crustal thickness

and velocities. Tomlinson *et al.* (2006) computed the crustal thickness from the teleseismic receiver functions analysis. The results from this work on the Moho depth broadly agree with the results from seismic reflection and refraction profiles (according to the authors,  $\pm 2$  km). Some receiver functions measurements from the stations close to the ISZ show a difference with other results of up to 5 km, but apart from this the Moho depths yielded by studies using different data types are generally consistent. One notable exception is the inconsistency regarding the crustal thickness in Wales, seen between our results and (e.g. Tomlinson *et al.* 2006; Maguire *et al.* 2011; Davis *et al.* 2012) with the Moho shallower in our model.

## 6 CONCLUSIONS

The resolving length of a model varies spatially and depends on the data sampling and errors in the data (Backus & Gilbert 1970). If the posterior model errors can be evaluated directly, then the optimal width of the averaging kernels—defined as the smallest width such that the error of the local average is below a specified threshold—can be determined at every point, and optimal resolution seismic tomography can be performed.

The optimal resolution tomography scheme described in this paper relies on the direct estimation of the model error at each point, which we implemented specifically for phase-velocity tomography. It then utilizes the fact that the errors of surface-wave phase-velocity maps increase nearly monotonically with the increasing map roughness. Thanks to this, an error threshold can be used as an effective

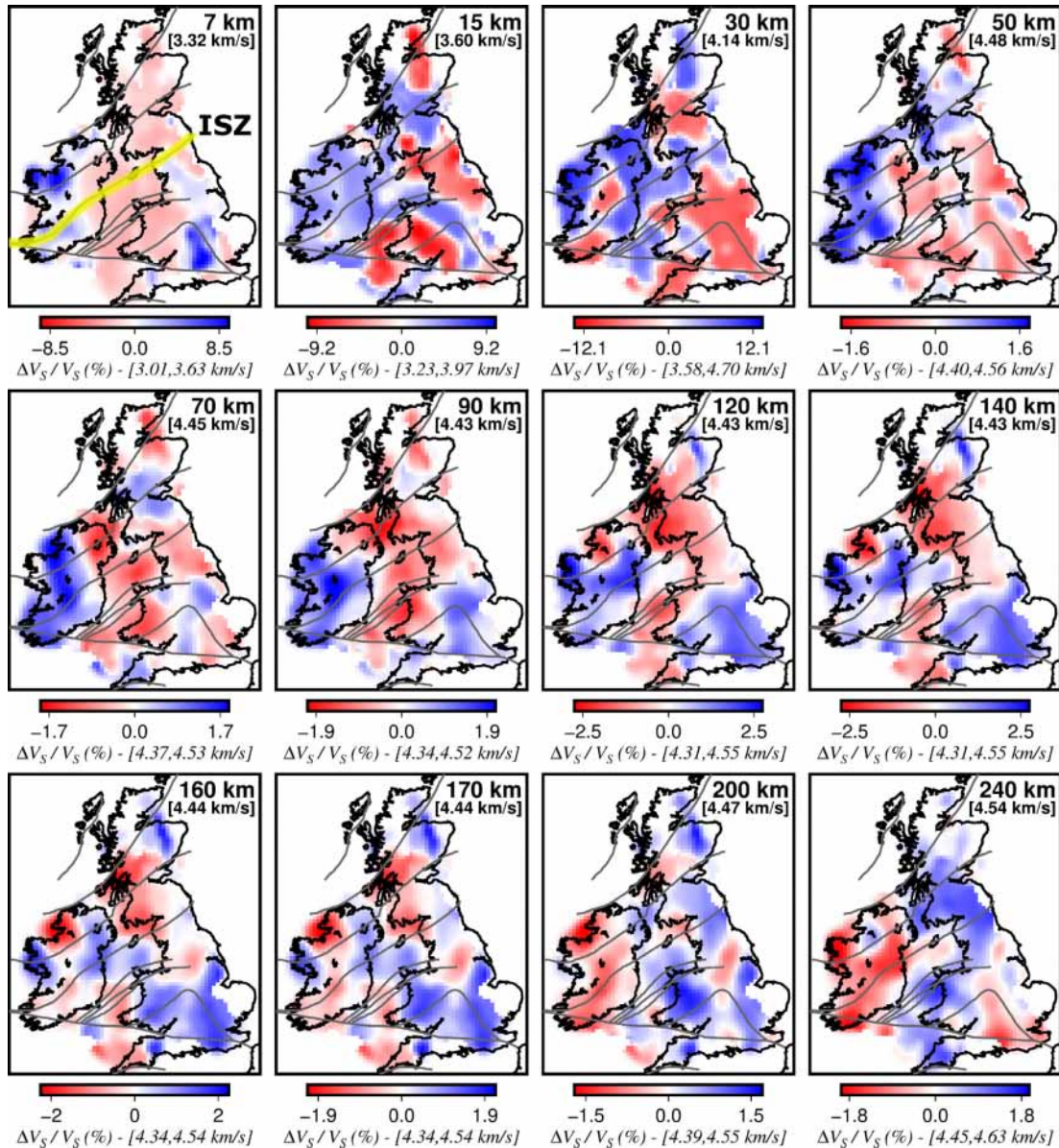


**Figure 23.** Shear-wave speed anomaly, plotted with respect to the region average at each depth. The grey lines represent major geological boundaries (after Tomlinson *et al.* 2006). The line highlighted in yellow represents the Iapetus Suture Zone (ISZ, e.g. Holland & Sanders 2009).

means of determining the optimal resolving length of the tomography at every point—that is, the optimal resolution.

The validity of the scheme depends on the actual resolution of the phase-velocity maps being similar at different periods, which we observe to be the case. At the longest periods, the resolution decreases, due to the increase of the wavelength of the waves, but this is mitigated by the decrease of the heterogeneity at the long periods.

Our large, new surface-wave data set from Ireland and Britain is characterized by unprecedentedly dense but highly heterogeneous data sampling. It also presents substantial systematic errors, evidenced by the best-sampled areas not always displaying the highest resolution. The application of the method to this data set has provided a rigorous test for it. Our optimal-resolution tomography

reveals strong, previously unknown lithospheric heterogeneity beneath Ireland and Britain and offers new insights into the structure and evolution of the region.

## ACKNOWLEDGEMENTS

We thank Nick Rawlinson for valuable comments on an early draft of the manuscript and the Editor, Andrea Morelli, and two anonymous reviewers for constructive suggestions that helped us to improve the paper. We are grateful to the operators of the networks and arrays in Ireland and Britain that produced the data used in this study: Ireland Array (Lebedev *et al.* 2012), the UK Seismograph Network operated by the British Geological Survey (Baptie 2018), INSN: the Irish National Seismic Network (INSN 1993; Blake *et al.* 2012), the Dublin



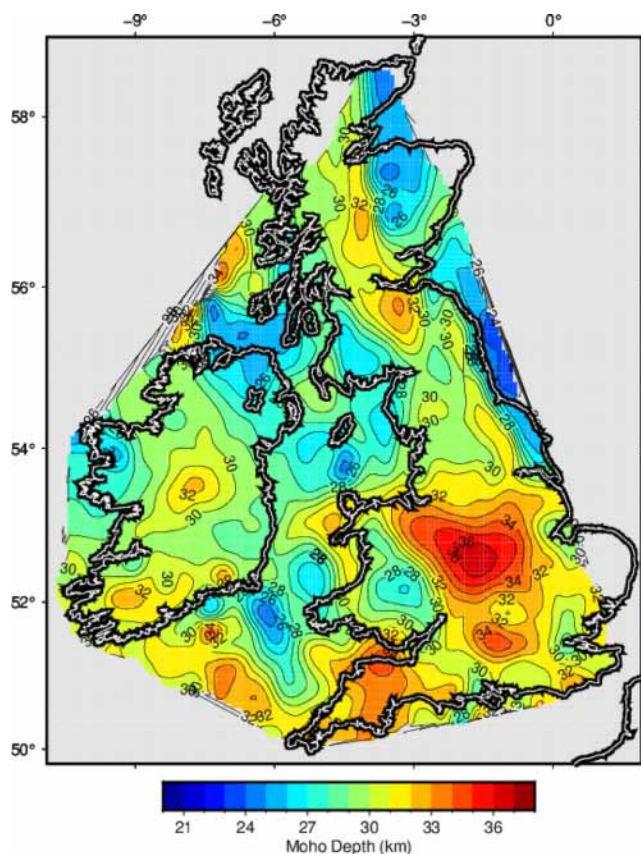


**Figure 24.** The Moho-depth map of the region yielded by the surface-wave tomography.

Basin temporary network (Licciardi & Piana Agostinetti 2014), the ISLE and ISUME projects (Landes *et al.* 2004; Do *et al.* 2006; Landes *et al.* 2007; Wawrzinek *et al.* 2008; O'Donnell *et al.* 2011; Polat *et al.* 2012), the WAVEOBS network (Möllhoff & Bean 2016), the SIM-CRUST project (Piana Agostinetti & Licciardi 2015), the Blacknest network (AWE 2020). The figures were created with the Generic Mapping Tools (GMT, Wessel *et al.* 2019). ISLE was funded by a Basic Research Grant SC/01/155 from Enterprise Ireland, and ISUME by a Research Frontiers Programme Research Grant 07/RFP/GE0758 from Science Foundation Ireland. This work was supported by research grants from Science Foundation Ireland (SFI) under grant number 13/CDA/2192 and grant number 13/RC/2092, cofunded under the European Regional Development Fund and by iCrag industry partners. Additional support came from grant 16/IA/4598, cofunded by the Science Foundation Ireland, the Geological Survey of Ireland and the Marine Institute.

## DATA AVAILABILITY

The waveform data from the Irish National Seismic Network (INSN) (<https://doi.org/10.7914/SN/EI>) are available from the international data centres (<http://geofon.gfz-potsdam.de/fdsnws/dataselect/1/>, <http://service.iris.edu/fdsnws>). The waveform data from Ireland Array will be available from the international data centres after a 1-year embargo period after the end of the project in 2021–2022. The waveform data from the UK Seismograph Network are available from the international data centres (<http://service.iris.edu/fdsnws>, <http://www.orfeus-eu.org/fdsnws>).

## REFERENCES

- Abbe, E., 1873. Beiträge zur theorie des mikroskops und der mikroskopischen wahrnehmung, *Archiv für mikroskopische Anatomie*, **9**(1), 413–468.
- Agius, M. & Lebedev, S., 2013. Tibetan and Indian lithospheres in the upper mantle beneath Tibet: evidence from broadband surface-wave dispersion, *Geochem. Geophys. Geosyst.*, **14**(10), 4260–4281.
- Agius, M. & Lebedev, S., 2014. Shear-velocity structure, radial anisotropy and dynamics of the Tibetan crust, *Geophys. J. Int.*, **199**, 1395–1415.
- Aki, K. & Lee, W., 1976. Determination of three-dimensional velocity anomalies under a seismic array using first p arrival times from local earthquakes: 1. A homogeneous initial model, *J. geophys. Res.*, **81**(23), 4381–4399.
- Al-Kindi, S., White, N., Sinha, M., England, R. & Tiley, R., 2003. Crustal trace of a hot convective sheet, *Geology*, **31**(3), 207–210.
- Arrowsmith, S.J., Kendall, M., White, N., VanDecar, J.C. & Booth, D.C., 2005. Seismic imaging of a hot upwelling beneath the British Isles, *Geology*, **33**(5), 345–348.
- Asencio, E., Knapp, J.H., Owens, T.J. & Helffrich, G., 2003. Mapping fine-scale heterogeneities within the continental mantle lithosphere beneath Scotland: Combining active- and passive-source seismology, *Geology*, **31**(6), 477–480.
- AWE, 2020. Awe blacknest, <https://www.awe.co.uk/about-us/our-locations>.
- Backus, G. & Gilbert, J., 1968. The resolving power of gross earth data, *Geophys. J. R. astr. Soc.*, **16**, 169–205.
- Backus, G. & Gilbert, J., 1970. Uniqueness in the inversion of inaccurate gross Earth data, *Phil. Trans. R. Soc. A.*, **266**(1173), 169–205.
- Bamford, D., Nunn, K., Prodehl, C. & Jacob, B., 1978. LISP IV. Crustal structure of northern Britain, *Geophys. J. R. astr. Soc.*, **54**, 43–60.
- Baptie, B., 2018. Earthquake seismology 2017/2018, Open Report or/18/029, British Geological Survey, doi:10.14470/TR560404.
- Barmin, M., Ritzwoller, M. & Levshin, A., 2001. A fast and reliable method for surface wave tomography, *Pure appl. Geophys.*, **158**, 1351–1375.
- Barton, P., 1992. LISP revisited: a new look under the Caledonides of northern Britain, *Geophys. J. Int.*, **110**, 371–391.
- Bartzsch, S., Lebedev, S. & Meier, T., 2011. Resolving the lithosphere-asthenosphere boundary with seismic Rayleigh waves, *Geophys. J. Int.*, **186**, 1152–1164.
- Bassin, C., Laske, G. & Masters, G., 2000. The current limits of resolution for surface-wave tomography in North America, *EOS, Trans. Am. geophys. Un.*, **81**.
- Bastow, I.D., Owens, T.J., Helffrich, G. & Knapp, J.H., 2007. Spatial and temporal constraints on sources of seismic anisotropy: evidence from the Scottish highlands, *Geophys. Res. Lett.*, **34**(5), doi:10.1029/2006GL028911.
- Baykiev, E., Guerri, M. & Fullea, J., 2018. Integrating gravity and surface elevation with magnetic data: mapping the curie temperature beneath the British Isles and surrounding areas, *Front. Earth Sci.*, **6**, 1–19.
- Becker, T.W. & Boschi, L., 2002. A comparison of tomographic and geodynamic mantle models, *Geochem. Geophys. Geosyst.*, **3**(1), doi:10.1029/2001GC000168.
- Bijwaard, H. & Spakman, W., 2000. Non-linear global P-wave tomography by iterated linearized inversion, *Geophys. J. Int.*, **141**, 71–82.
- Bijwaard, H., Spakman, W. & Engdahl, E.R., 1998. Closing the gap between regional and global travel time tomography, *J. geophys. Res.*, **103**(B12), 30 055–30 078.
- Blake, T., Lebedev, S., O'Reilly, B., Agostinetti, N., Agius, M. & Schaeffer, A., 2012. An unusual occurrence of a moderately sized earthquake (ml 4.2) on the Irish continental shelf and passive margin, *AGUFM*, S53A–2476.
- Bodin, T. & Sambridge, M., 2009. Seismic tomography with the reversible jump algorithm, *Geophys. J. Int.*, **178**, 1411–1436.
- Bodin, T., Sambridge, M., Tkalcic, H., Arroucau, P., Gallagher, K. & Rawlinson, N., 2012. Transdimensional inversion of receiver functions and surface-wave dispersion, *J. geophys. Res.*, **117**, doi:10.1029/2011JB008560.
- Bodin, T., Leiva, J., Romanowicz, B., Maupin, V. & Yuan, H., 2016. Imaging anisotropic layering with Bayesian inversion of multiple data types, *Geophys. J. Int.*, **206**(1), 605–629.

- Bonadio, R. *et al.*, 2018. Hot upper mantle beneath the Tristan da Cunha hotspot from probabilistic Rayleigh-wave inversion and petrological modeling, *Geochem. Geophys. Geosyst.*, **19**, 1412–1428.
- Boschi, L., 2003. Measures of resolution in global body wave tomography, *Geophys. Res. Lett.*, **30** (19), 25 567–25 594.
- Boschi, L. & Dziewonski, A., 1999. High-and low-resolution images of the Earth's mantle: implications of different approaches to tomographic modeling, *J. geophys. Res.*, **104**(B11), 25567–25594.
- Boschi, L., Weemstra, C., Verbeke, J., Ekström, G., Zunino, A. & Giardini, D., 2013. On measuring surface-wave phase velocity from station-station cross-correlation of ambient signal, *Geophys. J. Int.*, **192**, 346–358.
- Bott, M., Long, R., Green, A., Lewis, A., Sinha, M. & Stevenson, D., 1985. Crustal structure south of the Iapetus suture beneath northern England, *Nature*, **314**, 724–727.
- Brown, C. & Whelan, J.P., 1955. Terrane boundaries in Ireland inferred from the Irish Magnetotelluric Profile and other geophysical data, *J. geol. Soc. Lond.*, **152**, 523–534.
- Celli, N., Lebedev, S., Schaeffer, A., Ravenna, M. & Gaina, C., 2020. The upper mantle beneath the South Atlantic Ocean, South America and Africa from waveform tomography with massive data sets, *Geophys. J. Int.*, **221**, 178–204.
- Chadwick, R. & Pharaoh, T., 1998. The seismic reflection Moho beneath the United Kingdom and adjacent areas, *Tectonophysics*, **299**, 255–279.
- Chew, D.M. & Stillman, C.J., 2009. *Late Caledonian Orogeny and Magmatism*, Dunedin Academic Press Ltd.
- Chou, C. & Booker, J., 1979. A Backus–Gilbert approach to inversion of travel time data for three-dimensional velocity structure, *Geophys. J. R. astr. Soc.*, **59**, 325–344.
- Cogné, N., Doepke, D., Chew, D., Stuart, F.M. & Mark, C., 2016. Measuring plume-related exhumation of the British Isles in Early Cenozoic times, *Earth planet. Sci. Lett.*, **456**, 1–15.
- Constable, S., Parker, R. & Constable, C., 1987. Occam's inversion: a practical algorithm for generating smooth models from electromagnetic sounding data., *Geophysics*, **52**(3), 289–300.
- Curtis, A. & Snieder, R., 1997. Reconditioning inverse problems using the genetic algorithm and revised parameterization, *Geophysics*, **62**, 1524–1532.
- Dahlen, F. & Zhou, Y., 2006. Surface-wave group-delay and attenuation kernels, *Geophys. J. Int.*, **165**(2), 545–554.
- Dahlen, F.A. & Tromp, J., 1998. *Theoretical Global Seismology*, Princeton Univ. Press.
- Darbyshire, F.A. & Lebedev, S., 2009. Rayleigh wave phase-velocity heterogeneity and multilayered azimuthal anisotropy of the Superior Craton, Ontario, *Geophys. J. Int.*, **176**, 215–234.
- Davis, M., White, N., Priestley, K., Baptie, B. & Tilmann, F., 2012. Crustal structure of the British Isles and its epeirogenic consequences, *Geophys. J. Int.*, **190**, 705–725.
- De Laat, J., Celli, N. & Lebedev, S., 2019. Imaging the North Atlantic: deployment of the ocean-bottom seismometers of the SEA-SEIS project and quality control of global and regional network data, *Geophys. Res. Abstr.*, **21**, EGU2019-7548-3, 2019.
- de Vos, D., Paulssen, H. & Fichtner, A., 2013. Finite-frequency sensitivity kernels for two-station surface wave measurements, *Geophys. J. Int.*, **194**(2), 1042–1049.
- Debayle, E. & Sambridge, M., 2004. Inversion of massive surface-wave data sets: model construction and resolution assessment, *J. geophys. Res.*, **109**, doi:10.1029/2003JB002652.
- Demmerle, J., Wegel, E., Schermelleh, L. & Dobbie, I., 2015. Assessing resolution in super-resolution imaging, *Methods*, **88**, doi:10.1016/j.jmeth.2015.07.001.
- den Dekker, A. & van den Bos, A., 1997. Resolution: a survey, *J. Opt. Soc. Am. A*, **14**(3), 547–557.
- Deschamps, F., Lebedev, S., Meier, T. & Trampert, J., 2008. Azimuthal anisotropy of Rayleigh-wave phase velocities in the east-central United States, *Geophys. J. Int.*, **173**, 827–843.
- Di Leo, J., Bastow, I. & Helffrich, G., 2009. Nature of the Moho beneath the Scottish Highlands from a receiver function perspective, *Tectonophysics*, **474**, 214–222.
- Do, V., O'Reilly, B., Landes, M. & Readman, P., 2006. Shear-wave splitting observations across southwest Ireland, *Geophys. Res. Lett.*, **33**(L03309), 1–23 10.1029/2005GL024496.
- Dziewonski, A.M. & Anderson, D.L., 1981. Preliminary reference Earth model, *Phys. Earth planet. Inter.*, **25**, 297–356.
- Dziewonski, A.M., Hager, B.H. & O'Connell, R.J., 1977. Large-scale heterogeneities in the lower mantle, *J. geophys. Res.*, **82**(2), 239–255.
- Dziewonski, A.M., Chou, T.-A. & Woodhouse, J.H., 1981. Determination of earthquake source parameters from waveform data for studies of global and regional seismicity, *J. geophys. Res.*, **86**, 2825–2852.
- Edwards, J. & Blundell, D., 1984. Summary of seismic refraction experiments in the English Channel, Celtic Sea and St. George's Channel, Celtic Sea and St George's Channel, Marine Geophysics Report 144, British Geological Survey.
- Ekström, G., Nettles, M. & Dziewonski, A., 2012. The global CMT project 2004–2010: centroid-moment tensors for 13017 earthquakes, *Phys. Earth planet. Inter.*, **200–201**, 1–9.
- El-Sharkawy, A., Meier, T., Lebedev, S., Behrmann, J.H., Hamada, M., Cristiano, L., Weidle, C. & Köhn, D., 2020. The slab puzzle of the alpine-mediterranean region: Insights from a new, high-resolution, shear-wave velocity model of the upper mantle, *Geochem. Geophys. Geosyst.*, **21**(8), e2020GC008993.
- Endrun, B., Meier, T., Lebedev, S., Bohnhoff, M., Stavrakakis, G. & Harjes, H.-P., 2008. S velocity structure and radial anisotropy in the Aegean region from surface-wave dispersion, *Geophys. J. Int.*, **174**, 593–616.
- Erduran, M., Endrun, B. & Meier, T., 2008. Continental vs. oceanic lithosphere beneath the eastern Mediterranean Sea – implications from Rayleigh wave dispersion measurements, *Tectonophysics*, **457**, 42–52.
- Feynman, R., Leighton, R. & Sands, M., 1963. *The Feynman Lectures on Physics*, Mass: Addison-Wesley Pub. Co.
- Fitchner, A. & van Leeuwen, T., 2015. Resolution analysis by random probing, *JGR Solid Earth*, **120**(8), 5549–5573.
- Freeman, B., Klemperer, S. & Hobbs, R., 1988. The deep structure of northern England and the Iapetus Suture zone from BIRPS deep seismic reflection profiles, *J. geol. Soc. Lond.*, **145**, 727–740.
- Fry, B., Boschi, L., Ekstrom, G. & Giardini, D., 2008. Europe-Mediterranean tomography: high correlation between new seismic data and independent geophysical observables, *Geophys. Res. Lett.*, **35**(L04301), doi:10.1029/2007GL031519.
- Fukao, Y., Obayashi, M., Inoue, H. & Nebai, M., 1992. Subducting slabs stagnant in the mantle, *J. geophys. Res.*, **97**, 4809–4822.
- Fullea, J., Muller, M.R., Jones, A.G. & Afonso, J.C., 2014. The lithosphere-asthenosphere system beneath Ireland from integrated geophysical-petrological modeling II: 3D thermal and compositional structure, *Lithos*, **189**, 49–64.
- Galetti, E., Curtis, A., Baptie, B., Jenkins, D. & Nicolson, H., 2016. Trans-dimensional Love-wave tomography of the British Isles and shear-velocity structure of the East Irish Sea Basin from ambient-noise interferometry, *Geophys. J. Int.*, **208**, 36–58.
- GEOFON Data Centre, 1993. Geofon seismic network, *deutsches geoforschungszentrum gzf.* doi:10.14470/TR560404.
- Hardwick, A., 2008. New insights into the crustal structure of the England, Wales and Irish Seas areas from local earthquake tomography and associated seismological studies, *PhD thesis*, University of Leicester.
- Hawkins, R., Bodin, T., Sambridge, M., Choblet, G. & Husson, L., 2019. Trans-dimensional surface reconstruction with different classes of parameterization, *Geochem. Geophys. Geosyst.*, **20**(1), 505–529.
- Helmholtz, H., 1874. On the theoretical limits of the optical capacity of the microscope, *Mon. Microscop. J.*, **16**, 15–39.
- Hodgson, J., 2001. A seismic and gravity study of the Leinster Granite: SE Ireland, *PhD thesis*, Dublin Institute for Advanced Studies, Dublin, Ireland.
- Holland, C. & Sanders, I., 2009. *The Geology of Ireland*, 2nd edn, Dunedin Academic Press.

- INSN, 1993. Irish national seismic network, operated by the Dublin Institute For Advanced Studies and supported by the Geological Survey Ireland, International Federation of Digital Seismograph Networks, doi:10.7914/sn/ei.
- IOC, IHO, BODC, 2003. *Centenary Edition of the GEBCO Digital Atlas*, <https://www.gebco.net>.
- Jacob, A., Kaminski, W., Murphy, T., Phillips, W. & Prodehl, C., 1985. A crustal model for a northeast-southwest profile through Ireland, *Tectonophysics*, **113**(1–2), 75–103.
- Jones, A., Afonso, J., Fullea, J., Muller, M. & Salajegheh, F., 2013. The lithosphere–asthenosphere system beneath Ireland from integrated geophysical–petrological modeling – I: observations, 1D and 2D modelling, *Lithos*, **189**, 49–64.
- Jones, S.M., White, N., Clarke, B.J., Rowley, E. & Gallagher, K., 2002. Present and past influence of the Iceland Plume on sedimentation, *Geol. Soc., Lond., Spec. Publ.*, **196**, 13–25.
- Kelly, A., England, R.W. & Maguire, P.K., 2007. A crustal seismic velocity model for the UK, Ireland and surrounding seas, *Geophys. J. Int.*, **171**(3), 1172–1184.
- Kennett, B., Engdahl, E. & Buland, R., 1995. Constraints on seismic velocities in the Earth from traveltimes, *Geophys. J. Int.*, **122**(1), 108–124.
- Klemperer, S. & Hobbs, R., 1991. *The BIRPS Atlas: Deep Seismic Reflection Profiles Around the British Isles*, Cambridge Univ. Press.
- Klemperer, S., Ryan, P. & Snyder, D., 1991. A deep seismic reflection transect across the Irish Caledonides, *J. Geol. Soc. Lond.*, **148**, 149–164.
- Köhler, H., 1981. On abbe's theory of image formation in the microscope, *Opt. Acta: Int. J. Opt.*, **28**(12), 1691–1701.
- Kolínský, P., Bokelmann, G. & Group, A.W., 2021. On the wobbles of phase-velocity dispersion curves, *Geophys. J. Int.*, **224**(3), 1477–1504.
- Landes, M., Prodehl, C., Hauser, F., Jacob, A. & Vermeulen, N., 2000. VARNET-96: influence of the Variscan and Caledonian orogenies on crustal structure in SW Ireland, *Geophys. J. Int.*, **140**(3), 660–676.
- Landes, M., Ritter, J., Do, V., Readman, P. & O'Reilly, B., 2004. Passive teleseismic experiment explores the deep subsurface of southern Ireland, *EOS, Trans. Am. geophys. Un.*, **85**(36), 337–341.
- Landes, M., Ritter, J., Readman, P. & O'Reilly, B., 2005. A review of the Irish crustal structure and signatures from the Caledonian and Variscan orogenies, *Terra Nova*, **17**(2), 111–120.
- Landes, M., Ritter, J., O'Reilly, B., Readman, P. & Do, V., 2006. A N–S receiver function profile across the Variscides and Caledonides in SW Ireland, *Geophys. J. Int.*, **166**, 814–824.
- Landes, M., Ritter, J. & Readman, P., 2007. Proto-Iceland plume caused thinning of Irish lithosphere, *Earth planet. Sci. Lett.*, **255**(1), 32–40.
- Lebedev, S. & van der Hilst, R.D., 2008. Global upper-mantle tomography with the automated multimode inversion of surface and S-wave forms, *Geophys. J. Int.*, **173**, 505–518.
- Lebedev, S., Nolet, G. & van der Hilst, R.D., 1997. The upper mantle beneath the Philippine Sea region from waveform inversions, *Geophys. Res. Lett.*, **24**(15), 1851–1854.
- Lebedev, S., Chevrot, S. & van der Hilst, R.D., 2003. Correlation between the shear-speed structure and thickness of the mantle transition zone, *Phys. Earth planet. Inter.*, **136**(1–2), 25–40.
- Lebedev, S., Nolet, G., Meier, T. & van der Hilst, R.D., 2005. Automated multimode inversion of surface and S waveforms, *Geophys. J. Int.*, **162**, 951–964.
- Lebedev, S., Meier, T. & van der Hilst, R.D., 2006. Asthenospheric flow and origin of volcanism in the Baikal Rift area, *Earth planet. Sci. Lett.*, **249**, 415–424.
- Lebedev, S. *et al.*, 2012. Ireland Array: a new broadband seismic network targets the structure, evolution and seismicity of Ireland and surroundings, in *Proceedings of the EGU General Assembly 2012*, 22–27 April, Vienna, Austria, p. 3615.
- Lebedev, S., Adam, J. M.-C. & Meier, T., 2013. Mapping the Moho with seismic surface-waves: a review, resolution analysis, and recommended inversion strategies, *Tectonophysics*, **609**, 377–394.
- Licciardi, A. & Piana Agostinetti, N., 2014. High frequency receiver functions in the Dublin Basin: application to a potential geothermal site, *Ener. Proc.*, **59**, 221–226.
- Licciardi, A. & Piana Agostinetti, N., 2017. Sedimentary basin exploration with receiver functions: seismic structure and anisotropy of the Dublin Basin (Ireland), *Geophysics*, **82**, KS41–KS55.
- Licciardi, A., Piana Agostinetti, N., Lebedev, S., Schaeffer, A., Readman, P. & Horan, C., 2014. Moho depth and  $v_p/v_s$  in Ireland from teleseismic receiver functions analysis, *Geophys. J. Int.*, **199**, 561–579.
- Licciardi, A., England, R., Piana Agostinetti, N. & Gallagher, K., 2020. Moho depth of the British Isles: a probabilistic perspective, *Geophys. J. Int.*, **221**(2), 1384–1401.
- Lowe, C. & Jacob, A., 1989. A north-south seismic profile across the Caledonian Suture zone in Ireland, *Tectonophysics*, **168**, 297–318.
- Maguire, P., England, R. & Hardwick, A., 2011. LISPB DELTA, a lithospheric seismic profile in Britain: analysis and interpretation of the Wales and southern England section, *J. Geol. Soc.*, **168**(1), 61–82.
- Marquering, H. & Snieder, R., 1996. Surface-wave velocity structure beneath Europe, the northeastern Atlantic and western Asia from waveform inversion including surface wave mode coupling, *Geophys. J. Int.*, **127**, 238–304.
- Masson, F., Jacob, A., Prodehl, C., Readman, P., Shannon, P., Schulze, A. & Enderle, U., 1998. A wide-angle seismic traverse through the Variscan of southwest Ireland, *Geophys. J. Int.*, **134**, 689–705.
- Masson, F., Hauser, F. & Jacob, A., 1999. The lithospheric trace of the Iapetus Suture in SW Ireland from teleseismic data, *Tectonophysics*, **302**, 83–98.
- Masters, G., Barmine, M. & Kientz, S., 2007. Mineos user's manual, *Computational Infrastructure for Geodynamics*, California Institute of Technology, Pasadena, <http://geodynamics.org/cig/software/mineos>.
- Mather, B. & Fullea, J., 2019. Constraining the geotherm beneath the British Isles from Bayesian inversion of Curie depth: integrated modelling of magnetic, geothermal and seismic data, *Solid Earth*, **10**, 839–850.
- Mather, B., Farrell, T. & Fullea, J., 2018. Probabilistic surface heat flow estimates assimilating paleoclimate history: new implications for the thermochemical structure of Ireland, *J. geophys. Res.*, **123**(12), 10 951–10 967.
- McNaught, A. & Wilkinson, A., 2014. Resolution, Compendium of chemical terminology Gold Book, version 2.3.3, 1296.
- Meier, T., Dietrich, K., Stockhert, B. & Harjes, H., 2004. One-dimensional models of shear wave velocity for the eastern Mediterranean obtained from the inversion of Rayleigh wave phase velocities and tectonic implications, *Geophys. J. Int.*, **156**(1), 45–58.
- Menke, W., 2012. *Geophysical Data Analysis: Discrete Inverse Theory*, Academic Press.
- Menke, W., 2015. Review of the generalized least squares method, *Surv. Geophys.*, **36**(1), 1–25.
- Michelini, A., 1995. An adaptive-grid formalism for traveltimes tomography, *Geophys. J. Int.*, **121**, 489–510.
- Möllhoff, M. & Bean, C., 2016. Seismic noise characterization in proximity to strong microseism sources in the Northeast Atlantic, *Bull. seism. Soc. Am.*, **106**(2), 464–477.
- Nicolson, H., Curtis, A., Baptie, B. & Galetti, E., 2012. Seismic interferometry and ambient noise tomography in the British Isles, *Proc. Geol. Assoc.*, **123**, 74–86.
- Nicolson, H., Curtis, A. & Baptie, B., 2014. Rayleigh wave tomography of the British Isles from ambient seismic noise, *Geophys. J. Int.*, **198**, 637–655.
- Nolet, G., 1985. A seismic tomography program for geological investigations, in *Joint Interpretation of Geophysical and Geological Data Applied to Lithospheric Studies*, NATO ASI Series (Series C: Mathematical and Physical Sciences), Vol. **338**, pp. 109–126, eds Giese, P., Roeder, D. & Nicolich, R., Springer.
- Nolet, G., 2008. *A Breviary of Seismic Tomography*, Cambridge Univ. Press, p. 324.
- O'Donnell, J.P., Daly, E., Tiberi, C., Bastow, I.D., O'Reilly, B.M., Readman, P.W. & Hauser, F., 2011. Lithosphere–asthenosphere interaction beneath Ireland from joint inversion of teleseismic P-wave delay times and GRACE gravity, *Geophys. J. Int.*, **184**(3), 1379–1396.



- Oldenborger, G. & Routh, P., 2009. The point-spread function measure of resolution for the 3-d electrical resistivity experiment, *Geophys. J. Int.*, **176**(2), 405–414.
- O'Reilly, B., Hauser, F., Jacob, A. & Shannon, P., 1996. The lithosphere below the Rockall trough: wide-angle seismic evidence for extensive serpentinisation, *Tectonophysics*, **255**, 1–23.
- O'Reilly, B.M., Hauser, F. & Readman, P.W., 2010. The fine-scale structure of upper continental lithosphere from seismic waveform methods: insights into Phanerozoic crustal formation processes, *Geophys. J. Int.*, **180**(1), 101–124.
- O'Reilly, B.M., Hauser, F. & Readman, P.W., 2012. The fine-scale seismic structure of the upper lithosphere within accreted Caledonian lithosphere: implications for the origins of the 'Newer Granites', *J. Geol. Soc.*, **169**(5), 561–573.
- Paige, C.C. & Saunders, M.A., 1987. LSQR: an algorithm for sparse linear equations and sparse least squares, *ACM Trans. Math. Software (TOMS)*, **9**, 43–71.
- Parker, R., 1994. *Geophysical Inverse Theory*, Princeton Univ. Press, p. 386.
- Pawlak, A., Eaton, D.W., Darbyshire, F., Lebedev, S. & Bastow, I.D., 2012. Crustal anisotropy beneath hudson bay from ambient noise tomography: evidence for post-orogenic lower-crustal flow?, *J. geophys. Res.*, **117**(B8), doi:10.1029/2011JB009066.
- Piana Agostinetti, N. & Licciardi, A., 2015. SIM-CRUST: seismic imaging and monitoring of the upper crust: exploring the potential low-enthalpy geothermal resources of Ireland, in *Proceeding of the 2015 World Geothermal Congress*.
- Piana Agostinetti, N. & Malinverno, A., 2010. Receiver function inversion by trans-dimensional Monte Carlo sampling, *Geophys. J. Int.*, **181**(2), 858–872.
- Piana Agostinetti, N., Giacomuzzi, G. & Malinverno, A., 2015. Local 3D earthquake tomography by trans-dimensional Monte Carlo sampling, *Geophys. J. Int.*, **201**(3), 1598–1617.
- Pijpers, F. & Thompson, M., 1994. The sola method for helioseismic inversion, *Astron. Astrophys.*, **281**, 231–240.
- Polat, G., Lebedev, S., Readman, P.W., O'Reilly, B.M. & Hauser, F., 2012. Anisotropic Rayleigh-wave tomography of Ireland's crust: implications for crustal accretion and evolution within the Caledonian Orogen, *Geophys. Res. Lett.*, **39**(L04302), doi:10.1029/2012GL051014.
- Rao, C., Jones, A. & Moorkamp, M., 2007. The geometry of the Iapetus Suture Zone in central Ireland deduced from a magnetotelluric study, *Phys. Earth planet. Inter.*, **161**(1–2), 134–141.
- Ravenna, M. & Lebedev, S., 2018. Bayesian inversion of surface-wave data for radial and azimuthal shear-wave anisotropy, with applications to central Mongolia and west-central Italy, *Geophys. J. Int.*, **213**, 278–300.
- Ravenna, M., Lebedev, S., Fulla, J. & Adam, J. M.-C., 2018. Shear-wave velocity structure of southern Africa's lithosphere: variations in the thickness and composition of cratons and their effect on topography, *Geochem. Geophys. Geosyst.*, **19**, 1499–1518.
- Rawlinson, N. & Kennett, B., 2004. Rapid estimation of relative and absolute delay times across a network by adaptive stacking, *Geophys. J. Int.*, **157**(1), 332–340.
- Rawlinson, N. & Spakman, W., 2016. On the use of sensitivity tests in seismic tomography, *Geophys. J. Int.*, **205**(2), 1221–1243.
- Rawlinson, N., Pozgay, S. & Fishwick, S., 2010. Seismic tomography: a window into deep Earth, *Phys. Earth planet. Inter.*, **178** (3–4), 101–135.
- Rayleigh, J., 1896. On the theory of optical images, with special reference to the microscope, *Philos. Mag.*, **XLII**, 167–195.
- Readman, P., O'Reilly, B. & Murphy, T., 1997. Gravity gradients and upper-crustal tectonic fabrics, Ireland, *J. Geol. Soc. Lond.*, **154**, 817–828.
- Rickers, F., Fichtner, A. & Trampert, J., 2013. The Iceland–Jan Mayen plume system and its impact on mantle dynamics in the North Atlantic region: evidence from full-waveform inversion, *Earth planet. Sci. Lett.*, **367**, 39–51.
- Ritzwoller, M., Shapiro, N., Barmin, M. & Levshin, A., 2002. Global surface wave diffraction tomography, *J. geophys. Res.*, **107**(B12), ESE 4–1–ESE 4–13.
- Ronchi, V., 1961. Resolving power of calculated and detected images, *J. Opt. Soc. Am.*, **51**, 458–460.
- Sambridge, M. & Faletić, R., 2003. Adaptive whole Earth tomography, *Geochem. Geophys. Geosyst.*, **4**, doi:10.1029/2001GC000213.
- Sambridge, M. & Rawlinson, N., 2005. Seismic tomography with irregular meshes, in *Seismic Earth: Array Analysis of Broadband Seismograms*, eds Levander, A. & Nolet, G., Vol. **157**, pp. 49–65, American Geophysical Union.
- Sambridge, M., Braun, J. & McQueen, H., 1995. Geophysical parameterization and interpolation of irregular data using natural neighbours, *Geophys. J. Int.*, **122**, 837–857.
- Sato, Y., 1955. Analysis of dispersed surface waves by means of Fourier transform I, *Bull. Earthq. Res. Instit.*, **33**, 33–47.
- Schaeffer, A., Lebedev, S. & Becker, T., 2016. Azimuthal seismic anisotropy in the Earth's upper mantle and the thickness of tectonic plates, *Geophys. J. Int.*, **207**, 901–933.
- Schaeffer, A.J. & Lebedev, S., 2013. Global shear speed structure of the upper mantle and transition zone, *Geophys. J. Int.*, **194**, 417–449.
- Schaeffer, A.J. & Lebedev, S., 2015. Global heterogeneity of the lithosphere and underlying mantle: a seismological appraisal based on multimode surface-wave dispersion analysis, shear-velocity tomography, and tectonic regionalization, in *Invited Review in: The Earth's Heterogeneous Mantle*, eds Khan, A. & Deschamps, F., pp. 3–46, Springer Geophysics, doi:10.1007/978-3-319-15627-9.
- Schivardi, R. & Morelli, A., 2009. Surface wave tomography in the European and Mediterranean region, *Geophys. J. Int.*, **177**, 1050–1066.
- Shaw Champion, M., White, N., Jones, S. & Priestley, K., 2006. Crustal velocity structure of the British Isles: a comparison of receiver, *Geophys. J. Int.*, **166**, 795–813.
- Sheriff, R. & Geldart, L., 1995. *Exploration Seismology*, Cambridge Univ. Press.
- Smith, M.L. & Dahlen, F.A., 1973. The azimuthal dependence of Love and Rayleigh wave propagation in a slightly anisotropic medium, *J. geophys. Res.*, **78**, 3321–3333.
- Snyder, D. & Flack, C., 1990. A Caledonian age for reflectors within the mantle lithosphere north and west of Scotland, *Tectonics*, **9**, 903–922.
- Soomro, R., Weidle, C., Cristiano, L., Lebedev, S. & Meier, T., 2016. Phase velocities of Rayleigh and Love waves in central and northern Europe from automated, broadband, inter-station measurements, *Geophys. J. Int.*, **204**(1), 517–534.
- Tarantola, A. & Nercessian, A., 1984. Three-dimensional inversion without blocks, *Geophys. J. R. astr. Soc.*, **76**, 299–306.
- Tiley, R., White, N. & Al-Kindi, S., 2004. Linking Paleogene denudation and magmatic underplating beneath the British Isles, *Geol. Mag.*, **141**(3), 345–351.
- Tomlinson, J.P., Denton, P., Maguire, P.K. & Booth, D.C., 2006. Analysis of the crustal velocity structure of the British Isles using teleseismic receiver functions, *Geophys. J. Int.*, **167**(1), 223–237.
- Trampert, J. & van Heijst, H.J., 2002. Global azimuthal anisotropy in the transition zone, *Science*, **296**(5571), 1297–1299.
- van der Hilst, R., Widiyantoro, S. & Engdahl, E., 1997. Evidence for deep mantle circulation from global tomography, *Nature*, **386**(6625), 578–584.
- Wawerzinek, B., Ritter, J.R., Jordan, M. & Landes, M., 2008. An upper-mantle upwelling underneath Ireland revealed from non-linear tomography, *Geophys. J. Int.*, **175**, 253–268.
- Weidle, C., Soomro, R., Cristiano, L. & Meier, T., 2013. Identification of response and timing issues at permanent European broadband stations from automated data analysis, *Adv. Geosci.*, **36**, 21–25.
- Wessel, P., Luis, J., Scharroo, R., Wobbe, F., Smith, W. & Tian, D., 2019. The generic mapping tools version 6, *Geochem. Geophys. Geosyst.*, **20**(11), 5556–5564.
- White, N. & Lovell, B., 1997. Measuring the pulse of a plume with the sedimentary record, *Nature*, **387**(6636), 888–891.
- Yanovskaya, T., 2005. Development of methods for surface wave tomography based on the Backus–Gilbert approach, *Selected Papers From Volume 32 of Vychislitel'naya Seysmologiya*, **7**, 5–16.
- Zaroli, C., 2016. Global seismic tomography using Backus–Gilbert inversion, *Geophys. J. Int.*, **207**(2), 876–888.
- Zaroli, C., 2019. Seismic tomography using parameter-free Backus–Gilbert inversion, *Geophys. J. Int.*, **218**, 619–630.

- Zaroli, C., Koelemeijer, P. & Lambotte, S., 2017. Toward seeing the Earth's interior through unbiased tomographic lenses, *Geophys. Res. Lett.*, **44**, 11399–11408.
- Zhang, X., Paulssen, H., Lebedev, S. & Meier, T., 2009. 3d shear velocity structure beneath the Gulf of California from Rayleigh wave dispersion, *Earth planet. Sci. Lett.*, **279**(3–4), 255–262.
- Zhao, D., 2004. Global tomographic images of mantle plumes and subducting slabs: Insight into deep Earth dynamics, *Phys. Earth planet. Inter.*, **146**(1–2), 3–34.

## APPENDIX

### A1 Data sources

Until 2010, there was only one broadband (recording both short and long—over 100 s—periods) seismic station on the island of Ireland, the permanent station DSB near Dublin, operated jointly by the GEOFON network (GEOFON Data Centre 1993) and the Dublin Institute for Advanced Studies. Another permanent station, VAL on Valentia Island, was wide-band (periods up to 30 s only) and a few short period stations were operated at different times in the Republic of Ireland (ROI) and Northern Ireland (NI). There were also two temporary deployments of wide-band (30 s) stations: the project ISLE (Irish Seismic Lithospheric Experiment, Landes *et al.* 2004, 2006; Do *et al.* 2006; Wawerzinek *et al.* 2008), with stations in SW Ireland from 2002 to 2005, and the project ISUME (Irish Seismological Upper Mantle Experiment, O'Donnell *et al.* 2011; Polat *et al.* 2012) that installed stations across Ireland in 2006, with some of these recording to this day.

In 2010–2012, Ireland Array (Lebedev *et al.* 2012) deployed 20 broadband (nominally, 120 s, but also recording periods of hundreds of seconds) stations across ROI, with most of the stations recording continuously until present. At the same time, the Irish National Seismic Network (INSN) was established and installed 5 new permanent broadband stations (making it 6 in total, including DSB, Blake *et al.* 2012). Broadband stations of the UK Seismograph Network operated by the British Geological Survey (BGS, Baptie 2018) are distributed across Britain and Northern Ireland and complete the broadband station coverage of the area.

Our data set includes all the data recorded by the broadband networks in Ireland and all the publicly available data from the broadband stations in Britain. We also used all the data from temporary, wide-band deployments in Ireland, including ISLE, ISUME, WaveOBS (60-s and 30-s stations, Möllhoff & Bean 2016), Dublin Basin array (30-s stations, Licciardi & Piana Agostinetti 2014, 2017) and SIM-CRUST (30-s stations, Piana Agostinetti & Licciardi 2015) and the publicly available data from temporary deployments in Britain, including the Blacknest Array (AWE 2020). In total, our measurements were made on data recorded between 1981 and 2018, but the bulk of the data is from the last decade. Thanks to the recent growth in the number of stations, especially in Ireland, our data set provides an unprecedentedly dense data coverage of the entire region (Fig. 3).

### A2 Additional figures

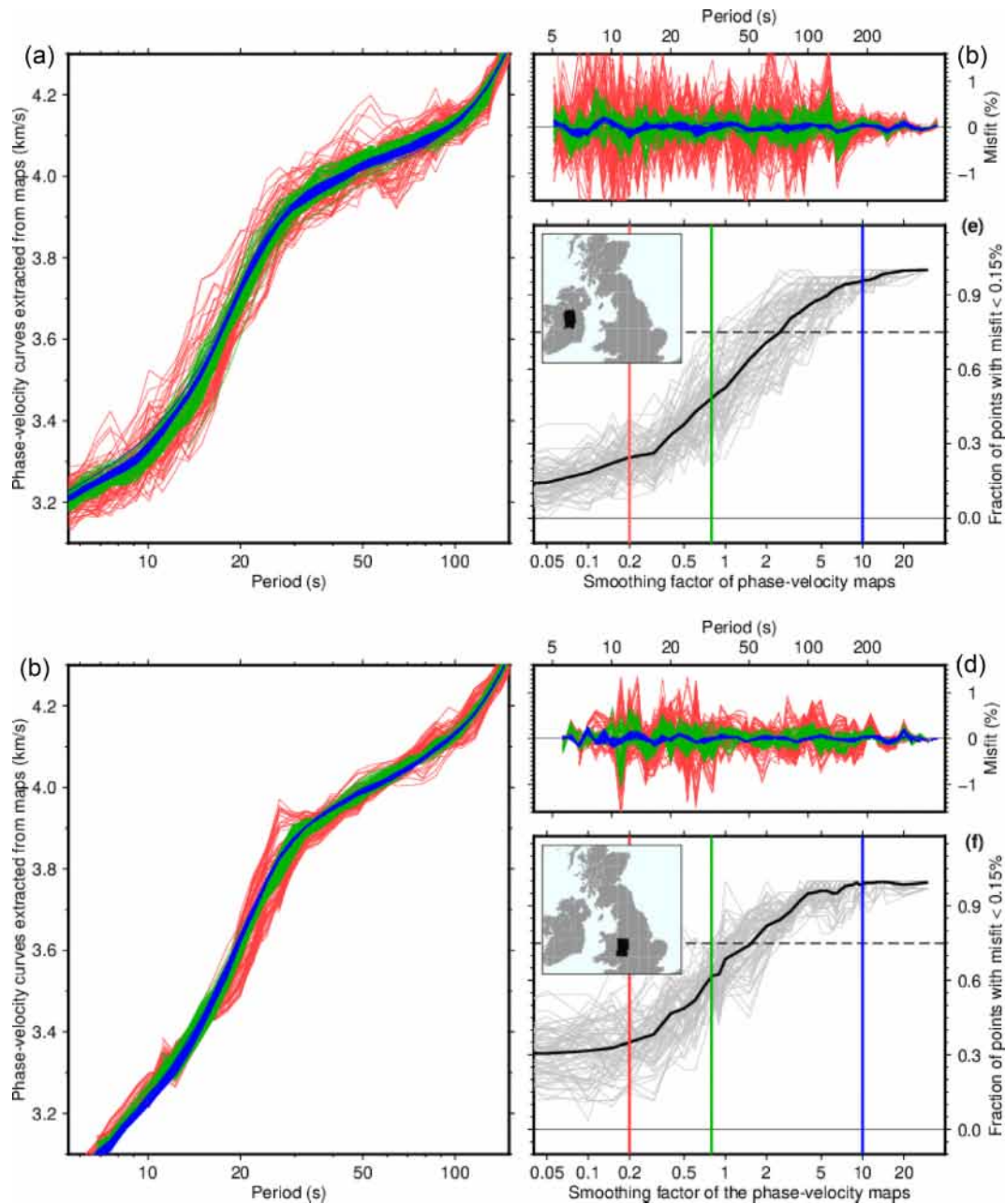


**Figure A1.** The decrease in the errors of phase-velocity curves with the increasing smoothness of the phase-velocity maps that they are derived from. The errors are estimated from the roughness of the phase-velocity curves (the rapid phase-velocity oscillations with period that could not be explained by any Earth structure). Panels (a), (b): phase-velocity curves extracted from the phase-velocity maps computed with many different smoothing levels, grouped into rough (red), intermediate (green) and smooth (blue), at sets of neighbouring knots in Ireland and Britain (black dots in the maps). Panels (c), (d): the misfits that quantify the period-dependent roughness of the curves and, by inference, their errors. Panels (e), (f): the fraction of points with the misfit lower than 0.15 per cent as a function of the smoothing applied (grey curves). Black: the average across the sets of neighbouring points.



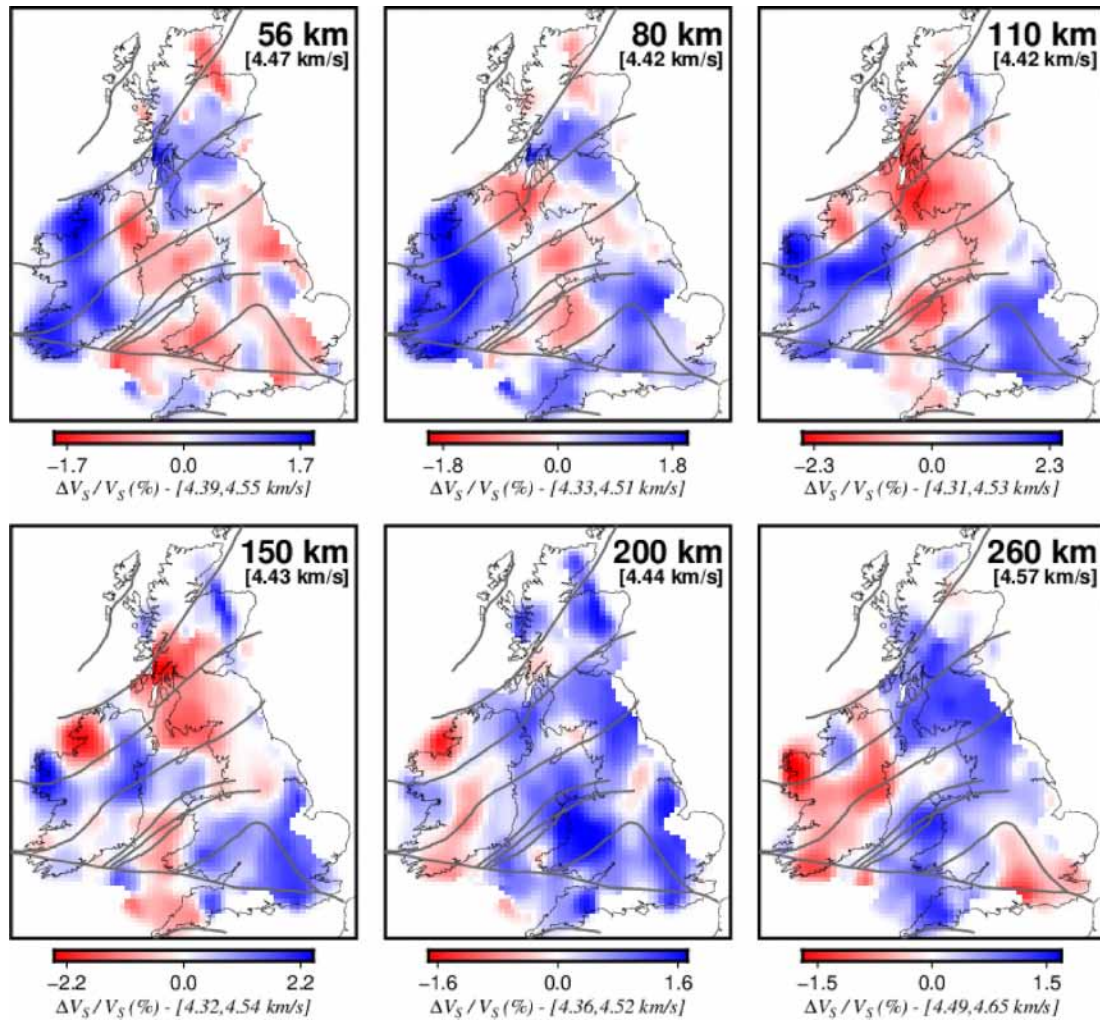
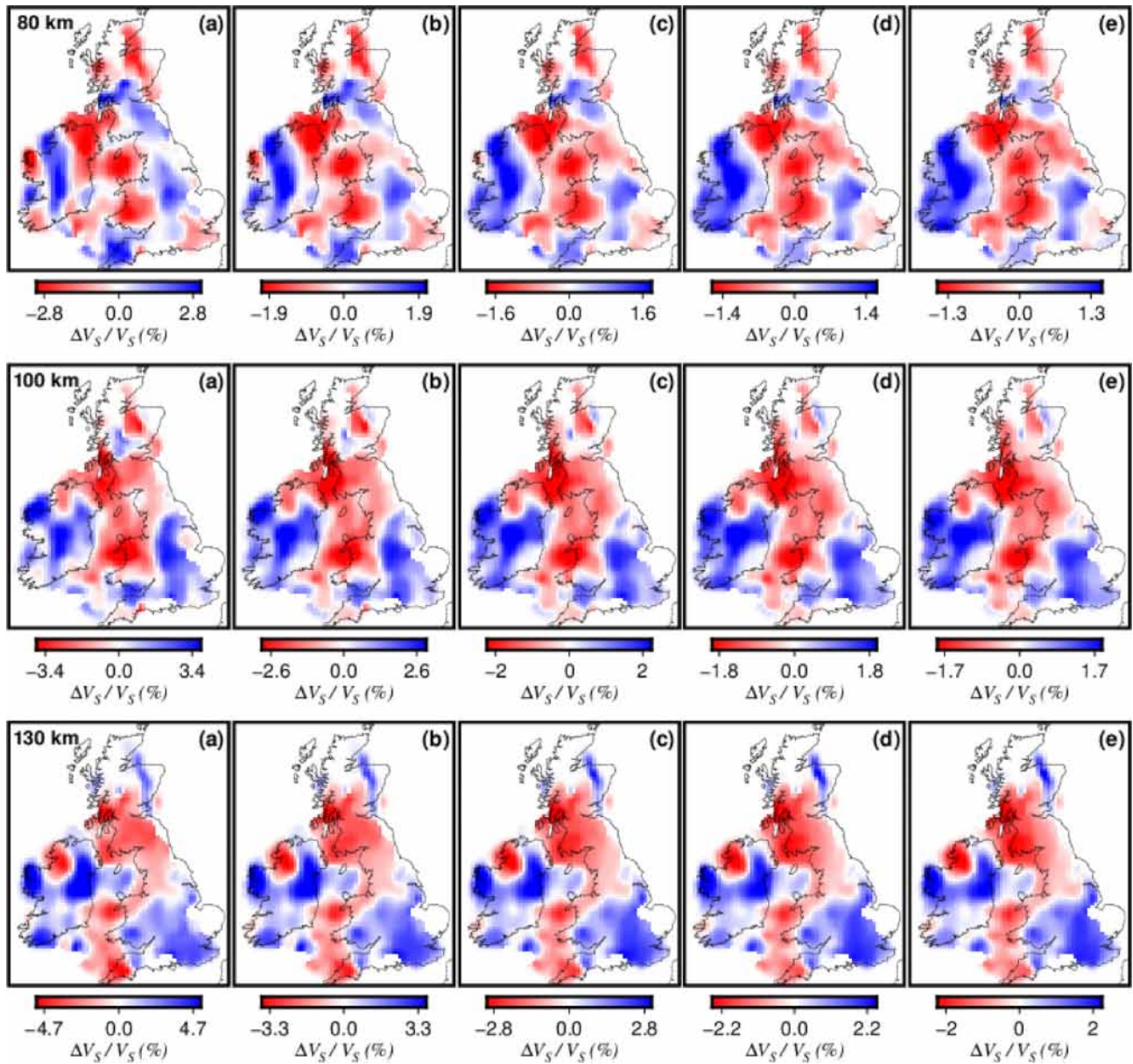


Figure A2. Shear-wave speed anomalies with respect to the global average values at the depths, taken from Schaeffer & Lebedev (2013).



**Figure A3.** Shear-wave models constructed using five different damping levels (increasing from (a) to (e) by a factor of 10) in the point-by-point, 1-D inversions, plotted at three different depths.